

Reliability of energy landscape analysis of resting-state functional MRI data

Pitambar Khanra¹, Johan Nakuci², Sarah Muldoon^{1,4}, Takamitsu Watanabe³, Naoki Masuda^{1,4,*}

¹ Department of Mathematics, State University of New York at Buffalo, Buffalo, USA.

² School of Psychology, Georgia Institute of Technology, Atlanta, USA

³ International Research Centre for Neurointelligence, The University of Tokyo, Japan

⁴ Institute for Artificial Intelligence and Data Science, State University of New York at Buffalo, Buffalo, USA

*corresponding author (naokimas@buffalo.edu)

Abstract

Energy landscape analysis is a data-driven method to analyze multidimensional time series, including functional magnetic resonance imaging (fMRI) data. It has been shown to be a useful characterization of fMRI data in health and disease. It fits an Ising model to the data and captures the dynamics of the data as movement of a noisy ball constrained on the energy landscape derived from the estimated Ising model. In the present study, we examine test-retest reliability of the energy landscape analysis. To this end, we construct a permutation test that assesses whether or not indices characterizing the energy landscape are more consistent across different sets of scanning sessions from the same participant (i.e., within-participant reliability) than across different sets of sessions from different participants (i.e., between-participant reliability). We show that the energy landscape analysis has significantly higher within-participant than between-participant test-retest reliability with respect to four commonly used indices. We also show that a variational Bayesian method, which enables us to estimate energy landscapes tailored to each participant, displays comparable test-retest reliability to that using the conventional likelihood maximization method. The proposed methodology paves the way to perform individual-level energy landscape analysis for given data sets with a statistically controlled reliability.

Key words: Maximum entropy model, Ising model, functional magnetic resonance imaging, Bayesian approximation, Permutation test, Fingerprinting

Number of words: 16938

Number of figures: 6

Number of tables: 13

Short title: Reliability of energy landscape analysis

List of abbreviations

ATN	attention network
CON	cingulo-opercular network
DMN	default mode network
EEG	electroencephalogram
FPN	fronto-parietal network
fMRI	functional magnetic resonance imaging
HCP	Human Connectome Project
ICA	independent component analysis
ICC	intraclass correlation coefficient
TSS	total sum of squares
MEG	magnetoencephalogram
MEM	maximum entropy model

MSC	Midnight Scan Club
ROI	region of interest
SAN	saliency network
SMN	somatosensory and motor network
VAN	ventral attention network

1. Introduction

Brain activity is dynamic and nonlinear in nature. Such nonlinear brain dynamics are considered to underlie many functions of the brain such as cognition, action, and learning [1–3], and mathematical modeling is widely accepted as a useful tool for simulating such brain dynamics on different scales [1–7]. There are also many methods for analyzing empirical data of neural dynamics, including dynamic causal modeling [8, 9], functional network analysis [10, 11], its dynamic variants [12–14], and hidden Markov models [15–17].

Population-level inferences are a common practice for analyzing brain activity in empirical data. However, both the structure and dynamics of the brain vary even among healthy individuals, let alone among individuals belonging to a disease group due to the heterogeneity of the disease. Therefore, although population-level inferences increase the data size and often help us to reach statistically significant observations, they may yield inaccurate results and loss of information when the observed data are individual-specific. To avoid population-level inferences, it is necessary to establish the reliability of individual-level inferences of collective brain dynamics.

Finn et al. examined the role of individual variability in functional networks measured by functional magnetic resonance imaging (fMRI) and its ability to act as a fingerprint to identify individuals [18] (see [19, 20] for earlier studies). In order for individual fingerprinting to be successful, the test-retest reliability of the functional network must be higher across sessions obtained from the same individual (i.e., within-participant reliability) than across sessions obtained from different individuals (i.e., between-participant reliability). Indeed, it was found that within-participant reliability was robust and that both resting-state and task fMRI from different sessions of the same individual could be used to perform fingerprinting [21]. Other studies also confirmed the ability of functional networks from fMRI data as fingerprints of individuals, including the development of different methods to quantify and improve fingerprinting [22–26]. The ability of functional connectivity to act as individual fingerprints has also been confirmed with electroencephalogram (EEG) [27] and magnetoencephalogram (MEG) data [28, 29].

Functional networks or its dynamic variants are not the only tools for analyzing brain dynamics or fingerprinting individuals. One way to analyze fMRI or other multidimensional time series data from the brain is to infer dynamics of discrete states. Each state may correspond to a particular functional network [13, 15, 30–33] or a spatial activation pattern [17, 34, 35], and the transition from one state to another may correspond to a regime shift in the brain. Energy landscape analysis is a method to characterize brain dynamics as a movement of a stochastic ball constrained on an energy landscape inferred from the data [36–38]. Quantifications of the estimated energy landscapes such as the height of the barrier between two local minima of the energy allow intuitive interpretations; a local minimum of the energy is a particular spatial activity pattern and defines a discrete brain state. A high barrier between two local minima implies that it is difficult for the brain dynamics to transit between the two local minima. Indices from energy landscape analysis have been shown to be associated with behavior of healthy individuals in a test of bistable visual perception task [37, 39], executive function [40], fluid intelligence [41], healthy aging [42], autism [43], Alzheimer disease [44], schizophrenia [45, 46], attention deficit hyperactivity disorder [47], and epilepsy [48].

These successful applications of energy landscape analysis are likely to owe to advantages of the method compared to other related methods such as functional network analysis and hidden Markov models. For example, with energy landscape anal-

ysis, one can borrow concepts and computational tools from statistical physics of spin systems to quantify the ease of state transition by the energy barrier [38] and complexity of the dynamics by different phases (e.g., spin-glass phase) and susceptibility indices [41]. In addition, each network state is by definition a binary activity pattern among a pre-specified set of regions of interest (ROIs) and therefore relatively easy to interpret. Despite its expanding applications, the validity of the energy landscape analysis has not been extensively studied except that one can measure the accuracy of fit of the model to the given data [38, 49–52]. A high accuracy of fit does not imply that the estimated energy landscape is a reliable fingerprint for individuals. In fact, if fMRI data are nonstationary, an energy landscape estimated for the same individual in two time windows may be substantially different from each other, whereas the accuracy of fit may be high in both time windows. Furthermore, the original energy landscape analysis method requires pooling of fMRI data from different individuals unless the number of regions of interest (ROIs) to be used is relatively small (e.g., 7) or the scanning session is extremely long. This is because the method is relatively data hungry [38]. The concept of individual fingerprinting is unclear when pooling of data is necessary.

The present study is a precursor to being able to assess individual differences. We assess potential utility of energy landscape analysis in individual fingerprinting by investigating its test-retest reliability. Specifically, we ask how much features of the estimated energy landscapes are reproducible across different sessions from the same individual as opposed to across sessions belonging to different sets of individuals. We hypothesize that test-retest reliability is higher between sessions for the same individual than between sessions for different individuals. Code for computing energy landscapes with the conventional and Bayesian methods is available on Github [53].

2. Methods

2.1. Midnight Scan Club data

We primarily use the fMRI data in the Midnight Scan Club (MSC) data set [22]. MSC data set contains five hours of resting-state fMRI data in total recorded from each of the 10 healthy human adults across 10 consecutive nights. A resting-state fMRI scanning session lasted for 30 minutes and yielded 818 volumes. Imaging was performed with a Siemens TRIO 3T MRI scanner using an echo planar imaging (EPI) sequence (TR = 2.2 s, TE = 27 ms, flip angle = 90°, voxel size = 4 mm × 4 mm × 4 mm, 36 slices).

The original paper reported that the eighth participant (i.e., MSC08) fell asleep, showed frequent and prolonged eye closures, and had systematically large head motion, resulting in much less reliable data than those obtained from the other participants [22]. We also noticed that the accuracy of fitting the energy landscape, which we will explain in section 2.4, fluctuated considerably across the different sessions for the tenth participant (i.e., MSC10), suggesting unstable quality of the MSC10’s data across sessions. Therefore, we excluded MSC08

and MSC10 from the analysis.

We used SPM12 (<http://www.fil.ion.ucl.ac.uk/spm>) to preprocess the resting-state fMRI data as follows: we first conducted realignment, unwrapping, slice-timing correction, and normalization to a standard template (ICBM 152); then, we performed regression analyses to remove the effects of head motion, white matter signals, and cerebrospinal fluid signals; finally, we conducted band-pass temporal filtering (0.01–0.1 Hz).

We determined the ROIs of the whole-brain network using an atlas with 264 spherical ROIs whose coordinates were set in a previous study [54]. We then removed 50 ROIs labelled ‘uncertain’ or ‘subcortical’, which left us with 214 ROIs. The 214 ROIs were labeled either of the nine functionally different brain networks, i.e., auditory network, dorsal attention network (DAN), ventral attention network (VAN), cingulo-opercular network (CON), default mode network (DMN), fronto-parietal network (FPN), salience network (SAN), somatosensory and motor network (SMN), or visual network. We merged the DAN, VAN, and CON into an attention network (ATN) to reduce the number of observables from nine to seven, as we did in our previous study [43]. This is due to the relatively short length of the data and the fact that energy landscape analysis requires sufficiently long data sets if working with 9 observables. In fact, the DAN, VAN, and CON are considered to be responsible for similar attention-related cognitive activity [54], justifying the merge of the three systems into the ATN. We call the obtained $N = 7$ dimensional time series of the fMRI signal the whole-brain network. We calculated the fMRI signal for each of the seven networks (i.e., ATN, auditory network, DMN, FPN, SAN, SMN, and visual network) by averaging the fMRI signal over the volumes in the sphere of radius 4 mm in the ROI and over all ROIs belonging to the network.

In addition to the whole-brain network, we used a separate 30-ROI coordinate system [55] and determined the multi-ROI DMN and CON. We used a different parcellation system for the DMN and CON than the 264-ROI system used for the whole-brain network. It is because the former (i.e., 30-ROI) coordinate system provides much fewer ROIs for the DMN and CON than the 264-ROI system does, which is convenient for energy landscape analysis. The original study identified 12 and 7 ROIs for the DMN and CON, respectively [55]. To reduce the dimension of the DMN, we averaged over each pair of the symmetrically located right- and left-hemisphere ROIs in the DMN into one observable. The symmetrized DMN, which we simply call the DMN, has eight ROIs because four ROIs (i.e., amPFC, vmPFC, pCC, and retro splen) in the original DMN are almost on the midline and therefore have not undergone the averaging between the right- and left-hemisphere ROIs [42]. For the CON, we used the original seven ROIs as the observables. Note that the whole-brain network contains the DMN and CON as single observables, whereas the DMN and CON we are introducing here are themselves systems containing $N = 8$ and $N = 7$ observables, respectively.

We denote the fMRI signal for the i th ROI at time t by x_i^t ($i = 1, \dots, N; t = 1, \dots, t_{\max}$), where N is the number of ROIs, and t_{\max} is the number of time points. We then removed the global signals and transformed the signals into their

z -values using $z_i^t = (x_i^t - m^t)/s^t$, where m^t and s^t represent the mean and standard deviation, respectively, of x_i^t over the N ROIs at time t ; m^t is the global signal [56]. The global signal in resting-state functional MRI data is considered to be dominated by physiological noise mainly originating from the respiratory, scanner-related, and motion-related artifacts. Global signal removal improves various quality-control metrics, enhances the anatomical specificity of functional-connectivity patterns, and can increase the behavioral variance [57, 58]. The same or similar global signal removal was carried out in previous energy landscape studies [41, 42].

2.2. Human Connectome Project data

For validation, we also analyzed fMRI data that were recorded from healthy human participants and shared as the S1200 data in the Human Connectome Project (HCP) [59]. In the data set, 1200 adults between 22–35 years old underwent four sessions of 15-min EPI sequence with a 3T Siemens Connectome-Skyra (TR = 0.72 s, TE = 33.1 ms, 72 slices, 2.0 mm isotropic, field of view (FOV) = 208 × 180 mm) and a T1-weighted sequence (TR = 2.4 s, TE = 2.14 ms, 0.7 mm isotropic, FOV = 224 × 224 mm). Here, we limited our analysis to those included in the 100 unrelated participant subset released by the HCP. We confirmed that all these 100 participants were among the subset of participants who completed diffusion weighted MRI as well as two resting-state fMRI scans.

The resting-state fMRI data of each participant are composed of two sessions, and each session is broken down into a Left-Right (LR) and Right-Left (RL) phases. We used data from participants with at least 1150 volumes in each of the four sessions after removing volumes with motion artifacts, which left us with 87 participants. For the 87 participants, we first removed the volumes with motion artifacts. Then, we used the last 1150 volumes in each session to remove possible effects of transient.

We used independent component analysis (ICA) to remove nuisance and motion signals [60]. Furthermore, any volumes with frame displacement greater than 0.2 mm [61] were excised [62] because the ICA-FIX pipeline has been found not to fully remove motion-related artifacts [63, 64]. We standardized each voxel by subtracting the temporal mean. Lastly, global signal regression of the same form as that for the MSC data (see section 2.1) was used for removing remaining noise.

In each volume, we averaged the fMRI signal over all the voxels within each ROI of the AAL atlas [65]. Note that this atlas is composed of 116 ROIs. Then, we mapped each cortical ROI to either of the parcellation scheme from the Schaefer-100 atlas [66]. System assignment was based on minimizing the Euclidian distance from the centroid of an ROI in the AAL to the corresponding centroid of an ROI in the Schaefer atlas. We removed 42 ROIs labeled ‘subcortical’ or ‘cerebellar’, which left us with 74 ROIs. These 74 ROIs were labelled either of the $N = 7$ functionally different brain networks: control network, DMN, DAN, limbic network, salience/ventral attention network, somatomotor network, and visual network, altogether defining a whole-brain network.

2.3. Fitting of the pairwise maximum entropy model

To carry out energy landscape analysis, we fit the pairwise maximum entropy model (MEM), also known as the Ising model, to the preprocessed fMRI data in essentially the same manner as in previous studies [38, 67].

For each session, we first binarized z_i^t for each i th ROI (with $i \in \{1, \dots, N\}$) and time t (with $t \in \{1, \dots, t_{\max}\}$) using a threshold that we set to the time average of z_i^t . A computational study showed that binarization did not affect important information contained in originally continuous brain signals [68]. We denote the binarized signal at the i th ROI and time t by σ_i^t , which is either +1 or -1 corresponding to whether z_i^t is larger or smaller than the threshold, respectively. The activity pattern of the entire network at time t is described by the N -dimensional vector

$$V^t = [\sigma_1^t, \dots, \sigma_N^t] \in \{-1, 1\}^N. \quad (1)$$

It should be noted that there are 2^N activity patterns in total, enumerated as V_1, \dots, V_{2^N} . The empirical mean activity at the i th ROI is denoted by

$$\langle \sigma_i \rangle \equiv \frac{1}{t_{\max}} \sum_{t=1}^{t_{\max}} \sigma_i^t. \quad (2)$$

The empirical mean pairwise joint activation for the i th and j th ROIs is defined by

$$\langle \sigma_i \sigma_j \rangle \equiv \frac{1}{t_{\max}} \sum_{t=1}^{t_{\max}} \sigma_i^t \sigma_j^t. \quad (3)$$

The pairwise MEM maximizes the entropy of the distribution of activity patterns under the condition that $\langle \sigma_i \rangle$ and $\langle \sigma_i \sigma_j \rangle$ (with $1 \leq i \leq j \leq N$) are the same between the estimated model and the empirical data. The resulting probability distribution of activity pattern $V = [\sigma_1, \dots, \sigma_N]$, denoted by $P(V)$, obeys the Boltzmann distribution [69] given by

$$P(V) = \frac{e^{-E(V)}}{\sum_{k=1}^{2^N} e^{-E(V_k)}}, \quad (4)$$

where $E(V)$ represents the energy of activity pattern V given by

$$E(V) = - \sum_{i=1}^N h_i \sigma_i - \frac{1}{2} \sum_{i=1}^N \sum_{j=1}^N J_{ij} \sigma_i \sigma_j. \quad (5)$$

In Eq. (5), the fitting parameter h_i represents the tendency for the i th ROI to be active (i.e., $\sigma_i = +1$), and J_{ij} quantifies the pairwise interaction between the i th and j th ROIs.

We denote the mean activity and mean pairwise activity from the estimated model by $\langle \sigma_i \rangle_m$ and $\langle \sigma_i \sigma_j \rangle_m$, respectively. By definition, we obtain

$$\langle \sigma_i \rangle_m = \sum_{k=1}^{2^N} \sigma_i(V_k) P(V_k) \quad (6)$$

and

$$\langle \sigma_i \sigma_j \rangle_m = \sum_{k=1}^{2^N} \sigma_i(V_k) \sigma_j(V_k) P(V_k). \quad (7)$$

We calculated h_i and J_{ij} by iteratively adjusting $\langle \sigma_i \rangle_m$ and $\langle \sigma_i \sigma_j \rangle_m$ towards the empirically values, i.e., $\langle \sigma_i \rangle$ and $\langle \sigma_i \sigma_j \rangle$, respectively, using a gradient ascent algorithm. The iteration scheme is given by

$$h_i^{\text{new}} = h_i^{\text{old}} + \epsilon \log \frac{\langle \sigma_i \rangle}{\langle \sigma_i \rangle_m} \quad (8)$$

and

$$J_{ij}^{\text{new}} = J_{ij}^{\text{old}} + \epsilon \log \frac{\langle \sigma_i \sigma_j \rangle}{\langle \sigma_i \sigma_j \rangle_m}, \quad (9)$$

where superscripts new and old represent the values after and before a single updating step, respectively, and ϵ is the learning rate. We set $\epsilon = 0.2$.

2.4. Accuracy of fit

We evaluated the accuracy of fit of the pairwise MEM to the given fMRI data [38, 42, 50]. The accuracy index is given by

$$r_D = \frac{D_1 - D_2}{D_1}, \quad (10)$$

where

$$D_\ell = \sum_{k=1}^{2^N} P_N(V_k) \log_2 \frac{P_N(V_k)}{P_\ell(V_k)} \quad (11)$$

is the Kullback-Leibler divergence between the probability distribution of the activity pattern in the ℓ th-order ($\ell = 1, 2$) MEM, $P_\ell(V)$, and the empirical probability distribution of the activity pattern, denoted by $P_N(V)$. Note that $P_2(V)$ is equivalent to $P(V)$ given by Eqs. (4) and (5). The first-order, or independent, MEM (i.e., $\ell = 1$) is Eq. (4) estimated without interaction terms, that is, $J_{ij} = 0 \forall i, j$ in Eq. (5). We obtain $r_D = 1$ when the pairwise MEM perfectly fits the empirical distribution of the activity pattern, and $r_D = 0$ when the pairwise MEM does not fit the data any better than the independent MEM.

To assess the dependency of r_D on the number of sessions to be concatenated for the estimation of the pairwise MEM, m , the network (i.e., whole-brain, DMN, or CON), and the type of concatenation (i.e., within-participant or between-participant), we examined the multivariate linear regression model given by

$$r_D = \beta_0 + \beta_1 m + \beta_2 I_{\text{whole}} + \beta_3 I_{\text{CON}} + \beta_4 I_{\text{within}}. \quad (12)$$

In Eq. (12), β_0 is the intercept, dummy variable I_{whole} is equal to 1 for the whole-brain network and 0 for the other two networks, I_{CON} is equal to 1 for the CON, and 0 for the other two networks, and I_{within} is equal to 1 for the within-participant comparison and 0 for the between-participant comparison.

2.5. Bayesian approximation method

The pairwise MEM and the subsequent energy landscape analysis have mostly been restricted to analysis of group-level data. This is because the methods in its original form are data-hungry, requiring concatenation of fMRI signals from different individuals. If there are sufficiently many or long sessions of fMRI data from a single participant, as in the present study, one can only concatenate the data from the same participant and thus avoid group-level energy landscape analysis. However, fMRI data from a single participant are more often than not too short to allow individual-level energy landscape analysis. In addition, the length of fMRI data, t_{\max} , that is necessary for reliably estimating the pairwise MEM with N nodes is roughly proportional to the number of states, 2^N [38]. To overcome this problem and obtain the energy landscape for each individual, we employed a recently developed variational Bayes approximation method for estimating the pairwise MEM [40, 70], which runs as follows.

We denote by \mathcal{S}_n the N -dimensional time series obtained from an n th session of fMRI. Different fMRI sessions typically originate from different participants in the same group (e.g., control group). We denote the number of sessions available by D . Let \mathcal{S} be the concatenated data, i.e.,

$$\mathcal{S} \equiv \bigcup_{n=1}^D \mathcal{S}_n. \quad (13)$$

The variational Bayes approximation method estimates a pairwise MEM for each \mathcal{S}_n (with $n \in \{1, \dots, D\}$).

This method introduces a prior distribution for the set of session-specific model parameters, $\theta_n = (h_1, h_2, \dots, h_N, J_{12}, J_{13}, \dots, J_{N-1,N}) \in \mathbb{R}^M$, where $n \in \{1, \dots, D\}$ and $M = N(N+1)/2$. We give the prior distribution for

$$\Theta = [\theta_1, \dots, \theta_D] \quad (14)$$

by

$$p(\Theta|\boldsymbol{\eta}, \boldsymbol{\alpha}) = \prod_{n=1}^D \prod_{M'=1}^M p(\theta_{nM'}|\mathcal{N}(\eta_{M'}, 1/\alpha_{M'})), \quad (15)$$

where $p(x|\mathcal{N}(\mu, \sigma^2))$ represents the probability density of x obeying the one-dimensional normal distribution with mean and variance equal to μ and σ^2 , respectively. Here, $\boldsymbol{\eta} = (\eta_1, \dots, \eta_M)^\top \in \mathbb{R}^M$ is the prior mean vector, $\boldsymbol{\alpha} = (\alpha_1, \dots, \alpha_M)^\top \in \mathbb{R}_+^M$ is the prior precision vector, and $^\top$ represents the transposition. In Eq. (15), we have assumed that the signals from all the D sessions are mutually independent.

Now, we derive the posterior distribution of Θ . It is intractable to derive the posterior because the normal distribution is not the conjugate prior for the Boltzmann distribution. Therefore, we use a variational approximation to the posterior [71] using the normal distribution as follows:

$$q(\Theta|\mathcal{S}, \boldsymbol{\eta}, \boldsymbol{\alpha}) = \prod_{n=1}^D \prod_{M'=1}^M p(\theta_{nM'}|\mathcal{N}(\mu_{nM'}, 1/\beta_{nM'})). \quad (16)$$

We write $\boldsymbol{\mu}_n = (\mu_{n1}, \dots, \mu_{nM})^\top \in \mathbb{R}^M$ and $\boldsymbol{\beta}_n = (\beta_{n1}, \dots, \beta_{nM})^\top \in \mathbb{R}_+^M$, which are the posterior mean vector

and the posterior precision vector for session $n \in \{1, \dots, D\}$, respectively. One obtains the variational approximate solution for distribution q by optimizing the evidence lower bound (ELBO), also called the free energy [40, 70]. By maximizing the free energy with respect to q , we have the posterior mean and precision vectors in terms of the prior mean and precision vectors as follows:

$$\boldsymbol{\mu}_n = \boldsymbol{\eta} + t_{\max} \mathbb{A}_{\boldsymbol{\eta}, \boldsymbol{\alpha}}^{-1} (\langle \bar{\sigma}_n \rangle - \langle \bar{\sigma} \rangle_{\boldsymbol{\eta}}), \quad (17)$$

$$\boldsymbol{\beta}_n = \boldsymbol{\alpha} + t_{\max} \mathbf{C}_{\boldsymbol{\eta}}, \quad (18)$$

where

$$\mathbb{A}_{\boldsymbol{\eta}, \boldsymbol{\alpha}} = \text{diag}(\boldsymbol{\alpha}) + t_{\max} \mathbf{C}_{\boldsymbol{\eta}}, \quad (19)$$

and $\text{diag}(\cdot)$ represents the diagonal matrix whose entries are given by the arguments. In Eq. (17), $\langle \bar{\sigma}_n \rangle \equiv (\langle \sigma_1 \rangle, \dots, \langle \sigma_N \rangle, \langle \sigma_1 \sigma_2 \rangle, \langle \sigma_1 \sigma_3 \rangle, \dots, \langle \sigma_{N-1} \sigma_N \rangle)^\top$ is the vector composed of the empirical mean activity and empirical pairwise joint activation; $\langle \bar{\sigma} \rangle_{\boldsymbol{\eta}}$ is the model mean of $\bar{\sigma}_n \equiv (\sigma_1, \sigma_2, \dots, \sigma_N, \sigma_1 \sigma_2, \sigma_1 \sigma_3, \dots, \sigma_{N-1} \sigma_N)^\top$ when the model parameters $(h_1, h_2, \dots, h_N, J_{12}, J_{13}, \dots, J_{N-1,N})$ are given by $\boldsymbol{\eta}$; $\mathbf{C}_{\boldsymbol{\eta}} \equiv \text{Cov}_{\boldsymbol{\eta}}(\bar{\sigma}_n)$ is the covariance matrix of $\bar{\sigma}_n$ when the model is given by $\boldsymbol{\eta}$. In Eq. (18), $\mathbf{C}_{\boldsymbol{\eta}}$ is the vector composed of the diagonal element of $\mathbf{C}_{\boldsymbol{\eta}}$. In other words, the i th element of $\mathbf{C}_{\boldsymbol{\eta}}$ is the variance of the i th element of $\bar{\sigma}_n$ under parameters $\boldsymbol{\eta}$.

Now, we fix q and maximize the free energy with respect to $\boldsymbol{\eta}$ and $\boldsymbol{\alpha}$ to obtain the equations for updating $\boldsymbol{\eta}$ and $\boldsymbol{\alpha}$ as follows:

$$\eta_{M'} = \frac{1}{D} \sum_{n=1}^D \mu_{nM'}, \quad (20)$$

$$\alpha_{M'} = \left[\frac{1}{D} \sum_{n=1}^D \left\{ (\mu_{nM'} - \eta_{M'})^2 + \frac{1}{\beta_{nM'}} \right\} \right]^{-1} \quad (21)$$

where $M' \in \{1, \dots, M\}$.

Thus, we have updated the posterior distribution $\theta_{nM'} \sim \mathcal{N}(\mu_{nM'}, 1/\beta_{nM'})$, $n \in \{1, \dots, D\}$, $M' \in \{1, \dots, M\}$ using the prior distribution $\theta_{nM'} \sim \mathcal{N}(\eta_{M'}, 1/\alpha_{M'})$, and then updated the prior distribution using the new posterior distribution. We summarize the steps of the variational Bayes approximation method as follows:

1. Initialize the hyperparameters by independently drawing each $\eta_{M'}$ (with $M' \in \{1, \dots, M\}$) from the normal distribution with mean 0 and standard deviation 0.1. We also set the first N entries of the prior precision vector $\alpha_{M'}$, corresponding to h_i , $i \in \{1, \dots, N\}$, to 6, and set the remaining $M - N$ entries of $\alpha_{M'}$ corresponding to J_{ij} , $1 \leq i < j \leq N$, to 30.
2. Calculate the posterior mean vector and posterior precision vector for each $n \in \{1, \dots, D\}$ using Eqs. (17) and (18).
3. Update the prior mean vector, $\boldsymbol{\eta} = (\eta_1, \dots, \eta_M)^\top$, and the prior precision vector, $\boldsymbol{\alpha} = (\alpha_1, \dots, \alpha_M)^\top$, using Eqs. (20) and (21).
4. If $\left| \frac{\text{ELBO}(\text{iter})}{\text{ELBO}(\text{iter}-1)} - 1 \right| < 10^{-8}$, we stop the iteration. Otherwise, we return to step 2. Here, $\text{ELBO}(\text{iter})$ represents the ELBO value after 'iter' iterations of steps 2 and 3.

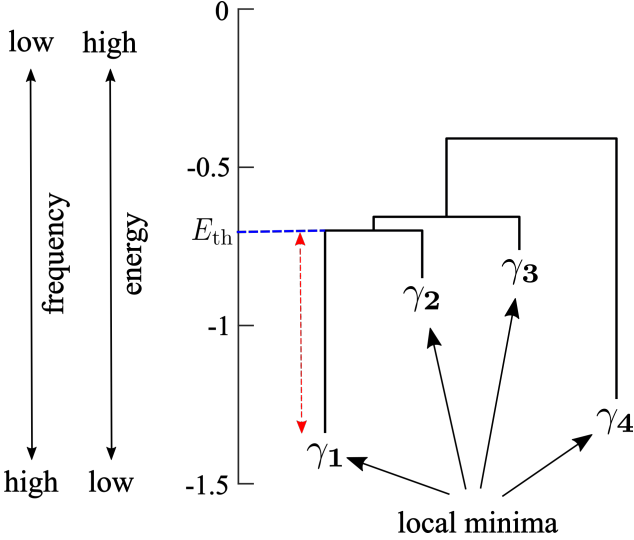


Figure 1: Schematic of a disconnectivity graph showing the relationships between the activity patterns that are energy local minima. The arrow indicates the height of the energy barrier between local minima γ_1 and γ_2 from the viewpoint of γ_1 .

2.6. Energy landscape and disconnectivity graph

Once we have estimated the pairwise MEM, we calculated the energy landscape [36–38, 42]. The energy landscape is defined as a network with 2^N nodes in which each node is an activity pattern. We first constructed a dendrogram called the disconnectivity graph. We show a hypothetical disconnectivity graph in Fig. 1. See Appendix A 9 for visualization of a real disconnectivity graph and its randomized counterpart. In the disconnectivity graph, a leaf corresponds to an activity pattern V_k that is a local minimum of the energy. There are four local minima in the disconnectivity graph shown in Fig. 1. The vertical position of the leaf represents the energy value of the local minimum. A low energy value corresponds to a high frequency of appearance through Eq. (5). For example, in Fig. 1, activity pattern γ_1 is the one that appears with the highest frequency among all the 2^N activity patterns.

By definition, activity pattern V_k is a local minimum of energy if and only if V_k appears more frequently (thus has a lower energy) than any other activity pattern adjacent to V_k . Two activity patterns are defined to be adjacent in the network of activity patterns if and only if they have the opposite activity $\sigma_i \in \{-1, 1\}$ for just one i . Note that the network of activity patterns is the hypercube composed of 2^N nodes in which each node representing an activity pattern is adjacent to N other nodes. To obtain the disconnectivity graph, we first enumerate the local minima. Then, for each pair of local minima γ and γ' , we determine the smallest energy value E_{th} that a path connecting γ and γ' needs to go through as follows. There may be various paths connecting γ and γ' . Then, we sequentially remove nodes in the descending order of the energy until there is no path connecting γ and γ' . The energy of the node that we have removed the last is the E_{th} value for γ and γ' . The horizontal dashed line in Fig. 1 indicates the E_{th} value ($= -0.69$)

for the pair of local minima γ_1 and γ_2 . The difference between E_{th} and the energy at the local minimum represents the energy barrier that the dynamics of the brain have to overcome to reach from one local minima to the other. In Fig. 1, the energy barrier between γ_1 and γ_2 from the viewpoint of γ_1 is 0.64, which is indicated by the double-headed arrow. The disconnectivity graph shows E_{th} and the energy barrier values for all pairs of the local minima.

2.7. Measures of discrepancy

To assess within-participant test-retest reliability of energy landscape analysis, we compared two energy landscapes that we separately estimated for two sets of fMRI data, which were in different sessions for the same participant or obtained from different participants. We decided to make within-participant versus between-participant comparisons because a successful individual fingerprinting requires that the within-participant test-retest reliability is high enough, whose examination requires a baseline. Higher within-participant test-retest reliability than between-participant one implies that the energy landscape analysis provides reliable fingerprints for individuals. To analyze test-retest reliability, we measured the following four indices of the discrepancy between the two energy landscapes.

2.7.1. Discrepancy in terms of the interaction strength

The energy landscape is primarily a function of $\{J_{ij}\}_{i,j \in \{1, \dots, N\}}$ because $\{h_1, \dots, h_N\}$ tend to take values close to 0 if we set our threshold to binarize z_i^t such that the fraction of $\sigma_i = -1$ and that of $\sigma_i = 1$ are not heavily imbalanced [41]. Therefore, we measured the discrepancy between two energy landscapes in terms of the estimated $\{J_{ij}\}$. We define the discrepancy using the Frobenius distance as follows:

$$d_J = \frac{2}{N(N-1)} \sum_{i=1}^N \sum_{j=i+1}^N \left| J_{ij}^{(1)} - J_{ij}^{(2)} \right|, \quad (22)$$

where $J^{(1)} = (J_{ij}^{(1)})$ and $J^{(2)} = (J_{ij}^{(2)})$ denote the pairwise interaction matrices according to the pairwise MEM estimated for the first and second data sets, respectively.

2.7.2. Discrepancy in terms of the activity patterns at the local minima of the energy

A local minimum of the energy landscape is locally the most frequent activity pattern. We compared the location of the local minima in the two energy landscapes by calculating the Hamming distance between the activity patterns at the local minima from the first energy landscape and those from the second energy landscape as follows.

First, we assumed that minor local minima characterized by low energy barriers with other local minima did not play important roles because the brain state would stay near such shallow local minima only briefly. Therefore, we started by removing minor local minima of the energy as follows. We generated

N random binary time series of length $4t_{\max}$ by independently drawing the $N \times 4t_{\max}$ binary numbers, i.e., -1 or $+1$, with the same probability (i.e., 0.5). The multiplication factor was set at 4 because we mainly analyzed energy landscapes of the empirical fMRI data with t_{\max} volumes that were concatenated over four sessions. Then, we inferred the pairwise MEM for the generated random binary time series and calculated the maximum length of the branch in the disconnectivity graph. A branch corresponds to a local minimum of the energy landscape. We define the branch length for local minimum γ by the smallest value of the energy barrier between γ and another local minimum γ' among all local minima $\gamma' (\neq \gamma)$. In the disconnectivity graph shown in Fig. 1, the branch length for γ_1 is the length of the arrow. We claim that the energy landscape estimated for the random binary time series, including the number and depth of its local minima, does not have functional meanings. Therefore, in an energy landscape estimated for the empirical data, the local minima whose branch length is comparable with the maximum branch length for the random binary time series are not important.

To implement this idea, we generated random binary time series, inferred the energy landscape, computed its maximum branch length, and repeated all these steps 100 times. We denote the average and standard deviation of the maximum branch length on the basis of the 100 random binary time series by μ' and σ' , respectively. We then identified the local minimum with the shortest branch length in the original disconnectivity graph. We removed that local minimum as being insignificant if its branch was shorter than $\mu' + 2\sigma'$. If we removed this local minimum, we recomputed the branch length of each local minimum whose branch had merged with the removed branch. Then, if the shortest branch was shorter than $\mu' + 2\sigma'$, we removed the branch and repeated these steps until all the local minima have branches whose length is at least $\mu' + 2\sigma'$. We refer to the local minima that survive this test as major local minima.

We denote the activity patterns at the major local minima of the first energy landscape by $\tilde{V}_1^{(1)}, \dots, \tilde{V}_{m_1}^{(1)}$, where m_1 is the number of the major local minima in the first energy landscape. Similarly, we denote the activity patterns at the major local minima of the second energy landscape by $\tilde{V}_1^{(2)}, \dots, \tilde{V}_{m_2}^{(2)}$. To examine similarity between $\{\tilde{V}_1^{(1)}, \dots, \tilde{V}_{m_1}^{(1)}\}$ and $\{\tilde{V}_1^{(2)}, \dots, \tilde{V}_{m_2}^{(2)}\}$, we need to match the major local minima between the two energy landscapes. To this end, we assume without loss of generality that $m_1 \leq m_2$ and pair each $\tilde{V}_\ell^{(1)}$ (with $\ell \in \{1, \dots, m_1\}$) with a $\tilde{V}_{\ell'}^{(2)}$ (with $\ell' \in \{1, \dots, m_2\}$) under the condition that different $\tilde{V}_\ell^{(1)}$'s are not matched to the same $\tilde{V}_{\ell'}^{(2)}$. We call the obtained correspondence between $\{\tilde{V}_1^{(1)}, \dots, \tilde{V}_{m_1}^{(1)}\}$ and $\{\tilde{V}_1^{(2)}, \dots, \tilde{V}_{m_2}^{(2)}\}$ a matching. Figure 2 describes how to match between the local minima of two energy landscapes.

Note that $m_2 - m_1$ major local minima in the second energy landscape are not matched to any major local minimum in the first energy landscape. We quantify the quality of a matching

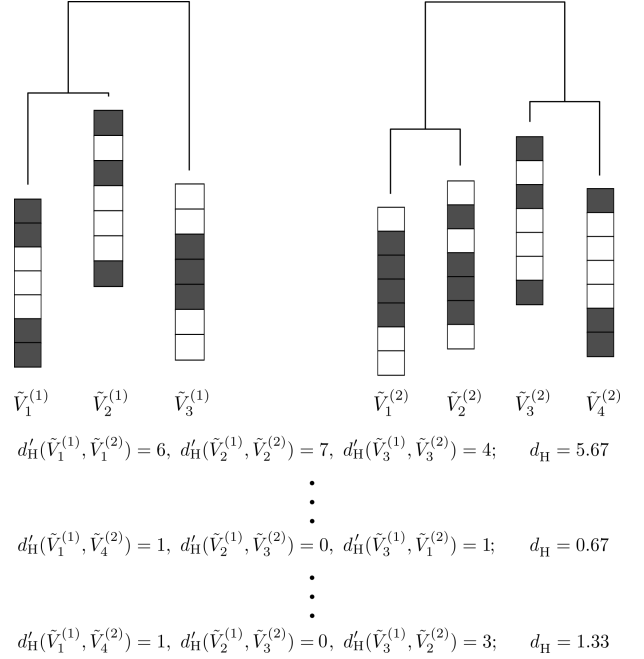


Figure 2: Schematic diagram describing how to match the local minima between two energy landscapes. In this example, there are three and four local minima in the first and second energy landscapes, respectively. With the first matching given by $\{(\tilde{V}_1^{(1)}, \tilde{V}_1^{(2)}), (\tilde{V}_2^{(1)}, \tilde{V}_2^{(2)}), (\tilde{V}_3^{(1)}, \tilde{V}_3^{(2)})\}$, we obtain $d_H = 5.67$. We calculate d_H for all the possible 24 matchings. The smallest d_H value is 0.67 . We adopt the matching that minimizes d_H , i.e., $\{(\tilde{V}_1^{(1)}, \tilde{V}_4^{(2)}), (\tilde{V}_2^{(1)}, \tilde{V}_3^{(2)}), (\tilde{V}_3^{(1)}, \tilde{V}_1^{(2)})\}$.

by

$$d_H = \frac{1}{m_1} \sum_{\ell=1}^{m_1} d_H'(\tilde{V}_\ell^{(1)}, \tilde{V}_{\rho(\ell)}^{(2)}), \quad (23)$$

where $\tilde{V}_{\rho(\ell)}^{(2)}$ is the activity pattern at the major local minimum paired with $\tilde{V}_\ell^{(1)}$ in the considered matching; d_H' is the Hamming distance between the N -dimensional binary vectors $\tilde{V}_\ell^{(1)}$ and $\tilde{V}_{\rho(\ell)}^{(2)}$, i.e., the number of ROIs whose binary activity (i.e., $\sigma_i = -1$ or $+1$) is opposite between $\tilde{V}_\ell^{(1)}$ and $\tilde{V}_{\rho(\ell)}^{(2)}$. We calculate d_H for all the possible matchings and select the one that minimizes d_H , which we simply refer to as d_H hereafter. A small d_H value implies that the two energy landscapes are similar in terms of the activity patterns at the local minima of energy.

2.7.3. Discrepancy in terms of the activity patterns averaged over the attractive basin

Brain dynamics tend to visit local minima of the energy landscape but also fluctuate around it. Therefore, we additionally measured a distance between the two energy landscapes in terms of the activity patterns averaged over the attractive basin of local minima as follows.

Consider a major local minimum of the first energy landscape, $\tilde{V}_\ell^{(1)}$. The attractive basin of $\tilde{V}_\ell^{(1)}$ is a set of activity patterns. By definition, V is in the attractive basin of $\tilde{V}_\ell^{(1)}$ if

and only if the gradient-descent walk starting from V eventually reaches $\tilde{V}_\ell^{(1)}$. The gradient-descent walk on the set of activity patterns is defined by a series of moves from an activity pattern to another such that the move from V is allowed only when the next activity pattern is the one that attains the smallest energy (i.e., largest probability of appearance) among the neighbors of V . Intuitively, if we release a ball at V , the ball following the gradient moves on the energy landscape until it reaches $\tilde{V}_\ell^{(1)}$ and stops there if there is no dynamical noise.

We calculate the average of the activity patterns within the attractive basin of $\tilde{V}_\ell^{(1)}$, which we denote by $\mathbf{u}_\ell^{(1)}$. Note that $\mathbf{u}_\ell^{(1)}$ is an N -dimensional vector, which we assume to be a column vector, whose i th entry is the average of $\sigma_i \in \{-1, 1\}$ over all the activity patterns in the attractive basin of $\tilde{V}_\ell^{(1)}$.

Similarly, denote by $\mathbf{u}_{\ell'}^{(2)}$ the average of the activity patterns in the attractive basin of $\tilde{V}_{\ell'}^{(2)}$ in the second energy landscape. Then, we calculate the cosine distance between $\mathbf{u}_\ell^{(1)}$ and $\mathbf{u}_{\ell'}^{(2)}$ given by

$$d'_{\text{basin}}(\mathbf{u}_\ell^{(1)}, \mathbf{u}_{\ell'}^{(2)}) = 1 - \frac{\mathbf{u}_\ell^{(1)\top} \mathbf{u}_{\ell'}^{(2)}}{\|\mathbf{u}_\ell^{(1)}\| \cdot \|\mathbf{u}_{\ell'}^{(2)}\|}, \quad (24)$$

where $\|\cdot\|$ denotes the Euclidean norm of the vector. The d'_{basin} value ranges between 0 and 2. A small value of d'_{basin} indicates a stronger alignment between $\mathbf{u}_\ell^{(1)}$ and $\mathbf{u}_{\ell'}^{(2)}$. For a given matching ρ , we then define

$$d_{\text{basin}} = \frac{1}{m_1} \sum_{\ell=1}^{m_1} d'_{\text{basin}}(\mathbf{u}_\ell^{(1)}, \mathbf{u}_{\rho(\ell)}^{(2)}), \quad (25)$$

which quantifies overall discrepancy between the two energy landscapes in terms of the average activity pattern in the attractive basin of the local minimum. We calculate d_{basin} for all the possible matchings between $\{\tilde{V}_1^{(1)}, \dots, \tilde{V}_{m_1}^{(1)}\}$ and $\{\tilde{V}_1^{(2)}, \dots, \tilde{V}_{m_2}^{(2)}\}$ and adopt the smallest value, which we also refer to as d_{basin} for simplicity. In a majority of cases, the best matching determined by the minimization of d_{H} and that determined by the minimization of d_{basin} are the same. However, they are sometimes different from each other.

2.7.4. Discrepancy in terms of the branch length

As a fourth measure to characterize energy landscapes, we quantified the ease with which the activity pattern switches from one major local minimum to another. We call it the normalized branch length. Then, we compared the normalized branch length between two energy landscapes.

We compute the normalized branch length as follows. We first calculate the length of the branch corresponding to each major local minimum γ as the difference between the energy value of γ and the smallest energy value at which γ joins the branch of another major local minimum on the disconnectivity graph. The calculated branch length quantifies the difficulty of transitioning from γ to another local minimum.

We assume that there are m_1 and m_2 major local minima from the first and second energy landscapes, respectively. We denote by $L^{(1)}$ and $L^{(2)}$ the average of the branch length over the m_1 corresponding branches in the first energy landscape and over the m_2 branches in the second energy landscape, respectively. Then, we define the normalized branch length difference between the two energy landscapes by

$$d_L = \frac{|L^{(1)} - L^{(2)}|}{\max(L^{(1)}, L^{(2)})}. \quad (26)$$

2.8. Nonparametric statistical analysis

We examine whether the energy landscapes estimated from different fMRI data from the same participants are more similar to each other than the energy landscapes estimated for two different groups of participants. We argue that, if the energy landscape analysis is useful, the energy landscapes estimated from the same participants should be closer to each other than the energy landscapes estimated from different participants.

First, we consider the MSC data with the conventional likelihood maximization method, for which we need to concatenate fMRI data over sessions to estimate one energy landscape with a reasonably high accuracy. For expository purposes, we consider one of the four discrepancy measures, say, d_J . We also focus on the p th participant. We first calculate d_J between $J^{(1)}$ and $J^{(2)}$, where we estimate $J^{(1)}$ for the fMRI data concatenated over four sessions that are uniformly randomly selected out of the ten sessions, $s \in \{1, \dots, 10\}$, and $J^{(2)}$ from the fMRI data concatenated over another uniformly randomly selected four sessions. We impose that the second set of four sessions does not overlap with the first set. Note that we use eight out of ten randomly selected sessions to calculate one d_J value. We repeat this procedure ten times to obtain ten values of d_J for the p th participant. By calculating ten values of d_J for each of the eight participants, i.e., $p \in \{1, \dots, 7, 9\}$, we obtain $8 \times 10 = 80$ values of d_J . We denote the average of the 80 values of d_J by d_1 (see Fig. 3(a)).

Next, we calculate d_J , with $J^{(1)}$ being estimated for the fMRI data concatenated over the s th sessions of four participants that are uniformly randomly selected out of the eight participants, and $J^{(2)}$ from the fMRI data concatenated over the s th sessions of the other four participants. We repeat this procedure ten times to obtain ten values of d_J for the s th session. By calculating the ten values of d_J for each of the ten sessions, i.e., $s \in \{1, \dots, 10\}$, we obtain $10 \times 10 = 100$ values of d_J . We denote the average of the 100 values of d_J by d_2 (see Fig. 3(a)).

Second, we consider the case in which we do not need to concatenate fMRI data before estimating an energy landscape. We again consider d_J as an example. We first calculate d_J between $J^{(1)}$ and $J^{(2)}$, where $J^{(i)}$, $i = \{1, 2\}$, is estimated for two sessions s and $s' (\neq s)$ for a participant p . It should be noted that $s, s' \in \{1, \dots, 10\}$ and $p \in \{1, \dots, 7, 9\}$ for the MSC data, and $s, s' \in \{1, \dots, 4\}$ and $p \in \{1, \dots, 87\}$ for the HCP data. By exhausting all pairs (s, s') , we compute n_1 values of d_J , where $n_1 = 10 \times 9/2 = 45$ and $n_1 = 4 \times 3/2 = 6$ for the MSC and HCP data, respectively, for each participant. We denote by

d_1 the average of the $8n_1$ or $87n_1$ values of d_J for the MSC or HCP data, respectively, which originate from all pairs (s, s') and all participants.

Next, we calculate d_J , with $J^{(1)}$ and $J^{(2)}$ being estimated for the s th session for two different participants p and p' ($\neq p$), where $p, p' \in \{1, \dots, 7, 9\}$ for the MSC data and $p, p' \in \{1, \dots, 87\}$ for the HCP data. By exhausting all pairs of participants (p, p') , we compute n_2 values of d_J , where $n_2 = 8 \times 7/2 = 28$ and $n_2 = 87 \times 86/2 = 3741$ for the MSC and HCP data, respectively, for each session. We denote by d_2 the average of the $10n_2$ or $4n_2$ values of d_J for the MSC or HCP data, respectively.

We define $ND \equiv d_2/d_1$; ND is named after normalized distance [72, 73]. If energy landscapes are more similar between different sets of sessions from the same participant (i.e., within-participant comparison) than between those from different participants (i.e., between-participant comparison), the ND value will be larger than 1. In this case, we regard that the energy landscape analysis bears high within-participant test-retest reliability. In contrast, if the energy landscape from the same participant is not particularly reliable across sessions, the ND will be close to 1.

To statistically examine whether ND is sufficiently larger than 1, we run a nonparametric permutation test, which is an adaptation of the same test in different studies [72, 73]. The steps of the permutation test based on the ND are as follows. Here we use d_J to explain the steps. See Fig. 3(b) for a schematic of randomized MSC data.

1. Consider the binarized N -dimensional fMRI time series data for each of the eight participants and each of the ten sessions.
2. Uniformly randomly permute the 80 participant-session pairs in the case of the MSC data or 348 ($= 87 \times 4$) participant-session pairs in the case of the HCP data. After the randomization, the fMRI data for the s th session from the p th participant is the fMRI data for a uniformly randomly selected session from a uniformly randomly selected participant without replacement.
3. We calculate ND for the randomized data. For the combination of the MSC data and the conventional likelihood maximization method, this step entails concatenating the fMRI data over four random sessions from the same participant p or over the s th sessions from four random participants, estimate the energy landscapes for the concatenated data, comparing two energy landscapes to calculate d_J , repeat this 80 times to obtain d_1 and 100 times to obtain d_2 , and compute $ND = d_2/d_1$. When the data are not concatenated (i.e., the MSC data with the variational Bayes method or the HCP data with the conventional method), we calculate d_J for each pair of sessions from the same participant p and take the average to obtain d_1 . We also calculate d_J for each pair of participants from each session s and take the average to obtain d_2 . Then, we set $ND = d_2/d_1$.
4. Repeat steps (2) and (3) over c random permutations, where c is a large number. We set $c = 10^3$.

5. Calculate the p value, which is the fraction of the random permutations that yield an ND value larger than that for the original data.
6. If the p value is significantly small, then we reject the null hypothesis that $d_1 = d_2$ in the original data. In this case, we conclude the significant presence of within-participant test-retest reliability in the energy landscape analysis.

In step 3, we calculate d_1 and d_2 as the within-participant and between-participant averages, respectively. However, for the randomized data, they are statistically the same except that d_1 and d_2 are averages of 80 and 100 values of d_J , respectively (for the case of the MSC data combined with the conventional likelihood maximization method). This is because d_J calculated for both d_1 and d_2 originates from the comparison of the energy landscape estimated from uniformly randomly selected four out of the 80 sessions and another uniformly randomly selected four sessions without overlapping. Therefore, d_1 and d_2 have the same mean, and ND is expected to be peaked approximately at 1. The present permutation test thus evaluates whether the reliability of the energy landscape analysis across sessions for the same participant is higher than that across sessions for different participants.

3. Results

3.1. Accuracy of fit of the pairwise MEM

We extracted N ROIs for three brain networks, i.e., the whole-brain network ($N = 7$), DMN ($N = 8$), and CON ($N = 7$). For each of them, we estimated the pairwise MEM for the resting-state fMRI signals obtained from healthy adults in the MSC data set.

We calculated r_D , the accuracy of fit of the pairwise MEM, for each pair of participant and session. We obtained $r_D = 69.12 \pm 6.41\%$ (average \pm standard deviation) for the whole brain network, $r_D = 57.97 \pm 8.94\%$ for the DMN, and $r_D = 77.65 \pm 5.41\%$ for the CON (also see Table 1).

Because the accuracy of fit is not high enough, as is customarily done, we concatenated the data across participants or across sessions, estimated the pairwise MEM, and calculated r_D [37, 38]. Specifically, we concatenated the fMRI data across m sessions, where $m \in \{2, 3, 4, 5\}$. The m sessions are from the same participant but from m different sessions, or have the same session ID (i.e., s) but from m different participants. We show in Table 1 the average and standard deviation of r_D for the three networks when we concatenated $m \in \{2, 3, 4, 5\}$ sessions from the same participant. Table 2 shows the r_D values when we concatenated m sessions from different participants. In both Tables 1 and 2, as expected, r_D increases as m increases ($\beta_1 = 3.09$ in Eq. (12); $p = 4.60 \times 10^{-9}$). Furthermore, r_D is larger with the within-participant than across-participant concatenation ($\beta_4 = 3.51$ in Eq. (12); $p = 6.04 \times 10^{-5}$). The latter result indicates that the energy landscape estimated through the within-participant concatenation of the fMRI data is more accurate than that estimated through the between-participant concatenation in terms of the accuracy of fit of the pairwise MEM.

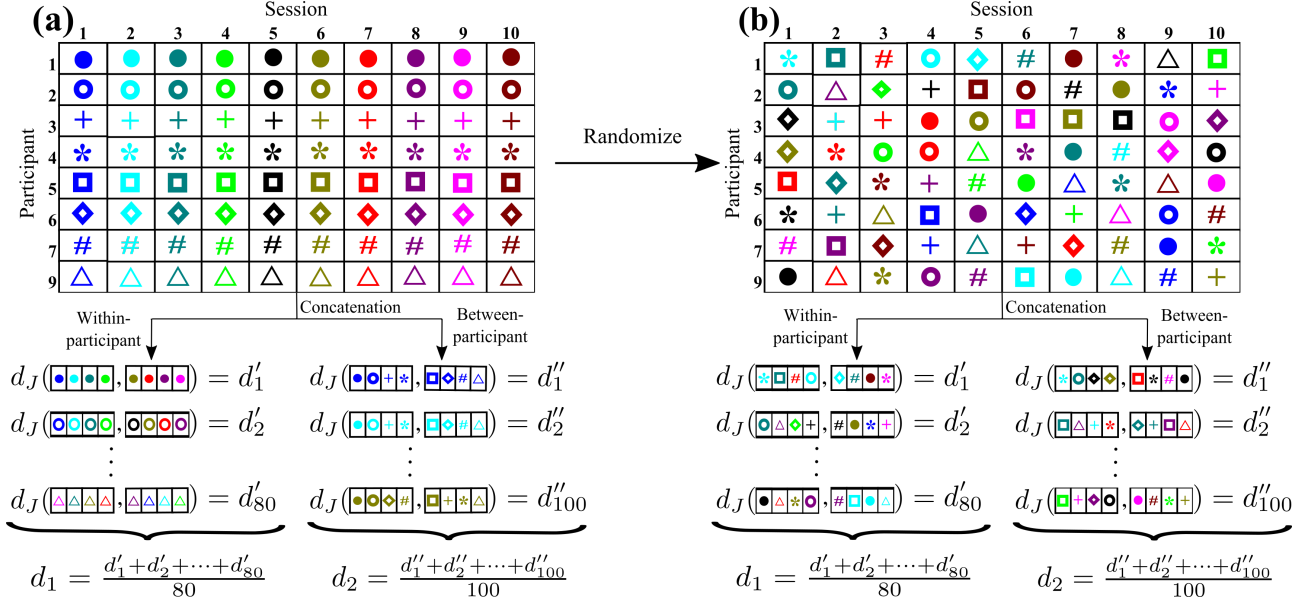


Figure 3: Schematic diagram describing concatenation of the fMRI data across different sessions and calculation of d_1 and d_2 . (a) For the original data. (b) For the randomized data. The inference of the energy landscape is based on the data concatenated across four sessions. The same four cells in the table are used for the concatenation in (a) and (b). However, because of the random permutation, any concatenation in (b) is over four sessions that are selected uniformly at random from the original data. Therefore, in (b), d'_1 and d''_1 , for example, are statistically the same, and the expectation of d_1 and that of d_2 are the same.

In both Tables 1 and 2, the accuracy for the DMN is substantially lower than that for the whole-brain network ($\beta_2 = 10.34$ in Eq. (12); $p = 1.63 \times 10^{-10}$) and the CON ($\beta_3 = 14.31$ in Eq. (12); $p = 5.54 \times 10^{-13}$). This is presumably because the DMN has one more ROI than the whole-brain network and the CON. The accuracy decreases as the number of ROIs increases in general [38].

In the following analyses, we use concatenation over $m = 4$ sessions and examine test-retest reliability of the energy landscape analysis. Figure 3(a) schematically explains the concatenation within each participant and that across participants. With $m = 4$, the accuracy of fit is more than 85% except for the DMN. In general, we are also interested in the test-retest reliability of fMRI data in the case of a relatively low accuracy of fit, which we test with the DMN. A concatenation over more sessions, such as with $m = 5$, would further increase the accuracy of fit (see Tables 1 and 2). Then, however, examining test-retest reliability may be more difficult because one needs to create two energy landscapes, preferably from non-overlapping data, and systematically compare them. In the present study, we use data obtained from eight participants. Therefore, if $m = 5$, one cannot avoid overlapping of the participants if we create two groups of participants for concatenating the fMRI data. Our choice of $m = 4$ balances the accuracy of fit and the tractability of the test-retest reliability analysis.

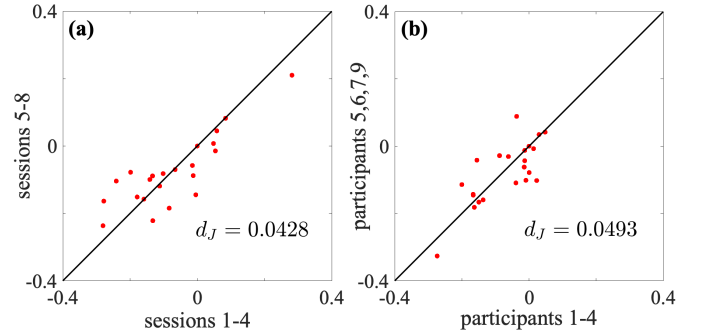


Figure 4: **Reliability of the interaction strength between two ROIs, J_{ij} , for the whole-brain network.** (a) Within-participant comparison. We concatenated the data for the first participant over four sessions. The horizontal and vertical axes correspond to the concatenation of sessions 1 to 4 and sessions 5 to 8, respectively. Each circle represents a pair of i and j . (b) Between-participant comparison. We concatenated the data from the first session over four participants. The horizontal and vertical axes correspond to the concatenation of the first and last four participants, respectively. In both (a) and (b), if all the circles lay on the diagonal, which we show by the solid lines, then the discrepancy, d_J , would be equal to 0. The d_J value is large if the circles tend to be far from the diagonal.

3.2. Reliability in terms of the interaction strength

We first examined the test-retest reliability of the energy landscape analysis in terms of the interaction strength parameters $\{J_{ij}\}$. We concatenated the fMRI data over the first four sessions from the p th participant and estimated $\{J_{ij}\}$ for each $p \in \{1, 2, 3, 4, 5, 6, 7, 9\}$. Similarly, for each participant p , we concatenated the data over the next four sessions (i.e., sessions 5 to 8) and estimated $\{J_{ij}\}$. For the whole-brain network, we

Reliability of energy landscape analysis of resting-state functional MRI data

m	Whole-brain network	DMN	CON
1	69.12 ± 6.41	57.97 ± 8.94	77.65 ± 5.41
2	81.26 ± 4.36	71.49 ± 5.77	86.26 ± 3.51
3	85.97 ± 3.34	76.78 ± 5.30	90.07 ± 2.32
4	88.62 ± 3.49	80.80 ± 4.44	92.30 ± 1.70
5	90.59 ± 2.45	83.73 ± 4.44	93.50 ± 1.54

Table 1: **Accuracy of fit of the pairwise MEM when we concatenate fMRI data within the same participant.** Each cell represents the accuracy of fit in percent when we concatenate the fMRI data across sessions from the same participant. We concatenated data from a given participant over m sessions and then fitted the pairwise MEM to the concatenated data. With $m = 2$, we partitioned the 10 sessions into 5 groups as (1,2), (3,4), (5,6), (7,8), and (9,10), concatenated the fMRI data within each group and within each participant, estimated the energy landscape, and computed the accuracy of fit, r_D . For example, we concatenated the data from the first two scanning sessions from participant 1, estimated the energy landscape, and computed r_D . We did the same for data from the third and fourth sessions from participant 1, the first and second sessions from participant 2, for example. With $m = 3$, we concatenated sessions $s = 1, 2$, and 3 from the same participant into one time series, sessions $s = 4, 5$ and 6 into one series, and sessions $s = 7, 8$, and 9 to one series. With $m = 4$, we concatenated sessions $s = 1, 2, 3$, and 4 into one series and sessions $s = 5, 6, 7$, and 8 into another series. With $m = 5$, we concatenated sessions $s = 1, 2, 3, 4$, and 5 into one series and sessions $s = 6, 7, 8, 9$, and 10 into another series. The average and standard deviation were computed across the participants and the different manners to concatenate m sessions per participant.

show the relationships between J_{ij} estimated for the first four sessions against that estimated for the next four sessions for the first participant in Fig. 4(a). Each circle represents J_{ij} for a pair of i and j . The values of $\{J_{ij}\}$ are reasonably consistent between the first four sessions and the next four sessions (Pearson correlation coefficient = 0.850; discrepancy $d_J = 0.0428$).

We instead concatenated the data for a single session over the first four participants (i.e., $p = 1, 2, 3$, and 4) and estimate $\{J_{ij}\}$, did the same for the last four participants (i.e., $p = 5, 6, 7$, and 9), and compared the two obtained sets of $\{J_{ij}\}$. In this manner, we investigated the consistency of the energy landscape between participants. For the whole-brain network, we show relationships between $\{J_{ij}\}$ for the two sets of participants in the first session in Fig. 4(b). Similar to the case of Fig. 4(a), the estimated $\{J_{ij}\}$ was reasonably consistent between the two concatenations, consistent with previous results with other data [42, 67, 74]. However, the degree of consistency was smaller for the present between-participant comparison (Pearson correlation coefficient = 0.773; discrepancy $d_J = 0.0493$) than the within-comparison comparison. In this particular example, the estimation of $\{J_{ij}\}$ was more consistent between pairs of sessions from the same participant than those from different participants.

To examine the generality of this result, we then calculated d_J between the concatenation across sessions 1 to 4 and that across sessions 5 to 8 from the same participant (i.e., within-participant comparison). The mean and standard deviation of

m	Whole-brain network	DMN	CON
1	69.12 ± 6.41	57.97 ± 8.94	77.65 ± 5.41
2	79.64 ± 3.77	64.71 ± 7.45	84.81 ± 3.68
3	83.92 ± 1.96	72.41 ± 4.51	86.66 ± 3.13
4	86.36 ± 1.85	73.46 ± 3.59	90.76 ± 2.07
5	87.51 ± 1.72	77.79 ± 3.23	91.27 ± 1.06

Table 2: **Accuracy of fit of the pairwise MEM when we concatenate fMRI data across different participants.** Each cell represents the accuracy of fit in percent when we concatenate the fMRI data across sessions from different participants. We concatenated data from a given session over m participants and then fitted the pairwise MEM to the concatenated data. With $m = 2$, we concatenated the data for the s th session from participants $p = 1$ and 2 into one time series, those from participants $p = 3$ and 4 into another series, those from participants $p = 5$ and 6 into another series, and those from participants $p = 7$ and 9 into another series. We did this for each s . With $m = 3$, we concatenated the data from participants $p = 1, 2$, and 3 into one series and those from participants $p = 4, 5$, and 6 into another series. With $m = 4$, we concatenated the data from participants $p = 1, 2, 3$, and 4 into one series and those from participants $p = 5, 6, 7$, and 9 into another series. With $m = 5$, we concatenated the data from participants $p = 1, 2, 3, 4$, and 5 into one series. Note that the results with $m = 1$ shown in this table are identical with those in Table 1. The average and standard deviation were computed across the sessions and the different manners to concatenate m participants given the session.

d_J over the eight participants were equal to $d_J = 0.0464 \pm 0.0082$ (mean \pm std) for the whole-brain network. We also calculated d_J between the concatenation of the s th session over the first four participants and that over the last four participants (i.e., between-participant comparison). The mean and standard deviation of d_J for the between-participant comparison over the ten sessions were equal to $d_J = 0.0527 \pm 0.0098$. We show these d_J values and those for the DMN and CON in Table 3. The table suggests that the energy landscape is apparently somewhat more similar between different fMRI sessions obtained from the same participant than between different participants.

To statistically investigate potential differences between the within-participant and between-participant comparisons, we carried out the permutation test on d_J . The ND for the whole-brain network, DMN, and CON were at least 1.3 (see Table 4). After a random permutation of the participants and sessions, the ND value was centered around 1 by definition. We show the distribution of the ND value obtained from $c = 10^3$ random permutations in Fig. 5(a), (b), and (c) for the whole-brain network, DMN, and CON, respectively. We calculated the p value for the empirical data by contrasting it to the distribution of ND for the randomized data. We obtained $p < 10^{-3}$ for all the three networks, implying that no random permutation yielded an ND value larger than that for the empirical data before the random permutation. These results remained significant after correction for the multiple comparison present in Table 4 ($p < 1.2 \times 10^{-2}$, Bonferroni corrected). Therefore, we conclude that the estimated parameter values, $\{J_{ij}\}$, are significantly more reliable in the within-participant than between-participant comparison

	Whole-brain network		DMN		CON	
	Within (d_1)	Between (d_2)	Within (d_1)	Between (d_2)	Within (d_1)	Between (d_2)
d_J	0.0464±0.0082	0.0527±0.0098	0.0448±0.0091	0.0634±0.0060	0.0432±0.0130	0.0684±0.0110
d_H	0.5800±1.0956	0.9125±0.8149	0.5417±0.4777	1.7333±1.0998	0.3854±0.4606	0.6667±0.3909
d_{basin}	0.0232±0.0239	0.0346±0.0329	0.0245±0.0220	0.0578±0.0245	0.0157±0.0098	0.0236±0.0121
d_L	0.2852±0.2100	0.3529±0.1625	0.2022±0.2366	0.3526±0.3341	0.2281±0.1679	0.3671±0.1683

Table 3: Discrepancy between two energy landscapes estimated by the conventional likelihood maximization applied to the MSC data. “Within” and “Between” in the table stand for within-participant and between-participant comparison, respectively. We computed the average and standard deviation of d_1 and d_2 across the participants and across the sessions, respectively.

	Whole-brain network	DMN	CON
d_J	ND = 1.315 $p < 10^{-3}$	ND = 1.415 $p < 10^{-3}$	ND = 1.580 $p < 10^{-3}$
d_H	ND = 1.934 $p < 10^{-3}$	ND = 3.200 $p < 10^{-3}$	ND = 1.730 $p < 10^{-3}$
d_{basin}	ND = 1.491 $p < 10^{-3}$	ND = 2.359 $p < 10^{-3}$	ND = 1.503 $p = 0.003$
d_L	ND = 1.237 $p = 0.014$	ND = 1.744 $p < 10^{-3}$	ND = 1.609 $p < 10^{-3}$

Table 4: ND values and the permutation test results for the four discrepancy measures, calculated with the conventional likelihood maximization applied to the MSC data. The p values are the uncorrected values.

for the three networks.

3.3. Reliability in terms of the activity patterns at the local minima

As a second index of the consistency between different energy landscapes, we compared the activity patterns at the local minima of the energy landscape between energy landscape pairs in terms of the Hamming distance, d_H . Table 3 indicates that the average d_H is at least 1.6 times larger for the between-participant than within-participant comparison for the whole-brain network, DMN, and CON.

The ND value was at least 1.73 for the three networks (see Table 4). The permutation test yielded $p < 10^{-3}$ for all the three networks; see Fig. 5(d)–(f) for the distribution of the ND values for the random permutations. These results altogether support that the reliability of the energy landscape analysis in terms of d_H is higher within the same participant than between different participants.

3.4. Reliability in terms of the activity patterns averaged over the attractive basin

As a third index to characterize the consistency between energy landscapes, we measured the distance between the average activity patterns belonging to the attractive basin of a local minimum in one energy landscape and that in another energy landscape, i.e., d_{basin} . Similarly to the case of d_J and d_H , we found that d_{basin} is substantially smaller for the within-participant than between-participant comparison for the three networks although the standard deviation is not small (see Table 3). It should be noted that the observed d_{basin} values are close to 0 for both the within-participant and between-participant comparisons. This result implies the almost full agreement between a pair of energy landscapes in terms of the averaged activity pattern in the attractive basin, even for the between-participant comparison.

We show in Fig. 5(g)–(i) for the distribution of the ND values for the random permutations as well as the ND values for the original energy landscapes. The permutation test yielded $p < 10^{-3}$ for the whole-brain network and the DMN and $p = 0.003$ for the CON (Table 4). These results support a significantly high test-retest reliability of the energy landscape analysis in terms of d_{basin} including the case of the CON after correction for multiple comparisons across the networks and indices ($p = 0.036$, Bonferroni corrected).

3.5. Reliability in terms of the branch length

As a last index of consistency of the energy landscape, we measure the normalized difference in the average branch length in the disconnectivity graph, d_L , between two energy landscapes. We found that the average of d_L was smaller for the within-participant than between-participant comparison for the three networks (see Table 3). The permutation test yielded $p = 0.014$ for the whole-brain network, and $p < 10^{-3}$ for the DMN and CON; see Table 4 and Fig. 5(j)–(l). These results support a significantly high test-retest reliability of the energy landscape analysis in terms of d_L for the DMN and CON although the result for the whole-brain network did not survive correction for multiple comparison ($p = 0.17$, Bonferroni corrected).

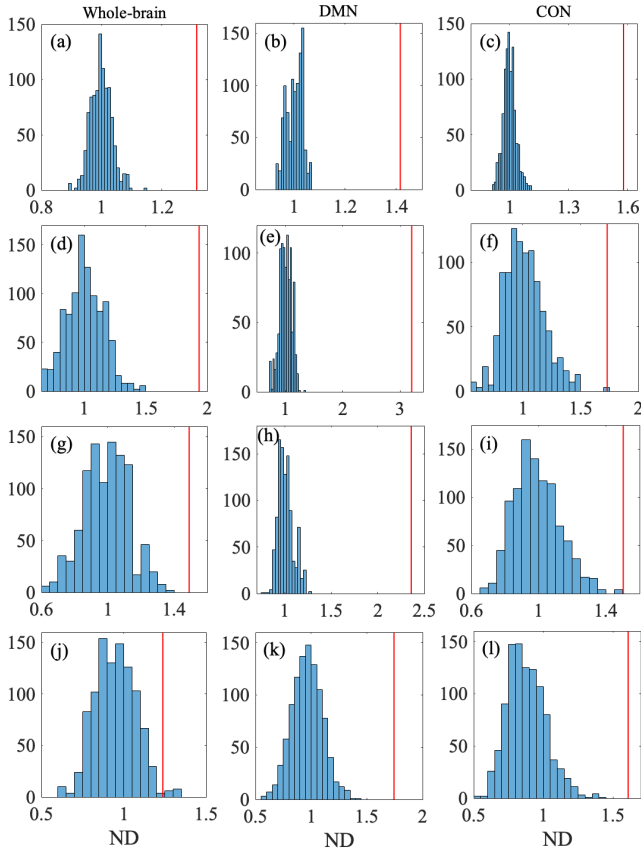


Figure 5: **Histogram of ND for the randomized data and the empirical ND value.** The first, second, and third columns of the figure show the distributions for the whole-brain network, DMN, and CON, respectively. The four rows of the figure show the distributions for d_J (in (a), (b), and (c)), d_H (in (d), (e), and (f)), d_{basin} (in (g), (h), and (i)), and d_L (in (j), (k), and (l)), from the top to the bottom. In each panel, the vertical line indicates the empirical ND value.

3.6. Accuracy and reliability of the variational Bayes approximation method

The Bayesian estimation potentially allows us to reliably estimate an energy landscape without concatenating fMRI data across sessions or participants even if a single session is not long. Therefore, we repeated the same test-retest reliability analysis on the MSC data with the Bayesian estimation and without any concatenation.

After running the variational Bayes approximation method to compute the hyperparameters, we calculated the accuracy of fit, r_D , of the pairwise MEM. We obtained $r_D = 86.02 \pm 2.79\%$, $91.50 \pm 3.21\%$, and $93.51 \pm 1.48\%$ for the whole-brain network, DMN, and CON, respectively. These high accuracy values support the effectiveness of the method.

We show the mean and standard deviation of the four discrepancy indices for the within-participant and between-participant comparison in Table 5. For some combinations of the session, participant, and network, the Bayesian method yielded an energy landscape with just one local (and hence global) minimum of the energy. In this case, we set the branch length to be 0. Table 5 suggests that the within-participant consistency of

energy landscape analysis is notably higher than the between-participant consistency in terms of the four discrepancy measures although the standard deviation is large. These results are qualitatively the same as those obtained with the conventional likelihood maximization method described in sections 3.2–3.5. However, the discrepancy values are substantially larger with the Bayesian method (see Table 5) than the likelihood maximization method (see Table 3) for both within-participant and between-participant comparisons with few exceptions.

Table 6 shows the results of the permutation test for the three networks and four discrepancy measures. We find significantly higher reliability within the same participant than between different participants in terms of d_J , d_H and d_{basin} . In terms of d_L , the uncorrected p values were smaller than 0.05 but did not survive the Bonferroni correction for the whole-brain network and DMN. These results were similar to those for the likelihood maximization method. However, comparison of Tables 4 and 6 reveals that the ND value with the Bayesian method was smaller than that with the likelihood maximization method for all the four discrepancy measures and all the three networks. Therefore, we conclude that the Bayesian method yields significantly higher reliability within the same participant than between different participants in most cases, whereas the reliability is somewhat weaker than in the case of the conventional likelihood maximization method.

3.7. Validation with the Human Connectome Project data

As a different type of validation, we ran the test-retest reliability analysis for another fMRI data set, HCP data. We used a whole-brain network with $N = 7$ ROIs. We calculated the accuracy of fit, r_D , of the pairwise MEM estimated with the likelihood maximization method to single-session data. We obtained $r_D = 92.49 \pm 1.99\%$, where we calculated the average and standard deviation on the basis of the four sessions per participant and all the participants. Table 7 shows the mean and standard deviation of the four discrepancy indices, compared between the within-participant and between-participant comparison. The results are similar to those for the MSC data. The ND values for d_J , d_H , d_{basin} , and d_L are 1.310, 1.152, 1.249, and 1.152, respectively. The permutation test yielded $p < 10^{-3}$ for all the four discrepancy indices. These results confirm significantly higher within-participant than between-participant test-retest reliability of the energy landscape analysis with a different data set.

3.8. Permutation test by shuffling the participants within each session

As another validation, we carried out a different variant of the permutation test in which we shuffled the participants within each session; the same shuffling was employed in previous studies [75, 76]. Most combinations of the discrepancy measure and the network showed significantly small p values after the Bonferroni correction for the different data sets and energy landscape inference methods. (See Appendix B 10 for the detailed methods and results.) This result is similar to the case of

	Whole-brain network		DMN		CON	
	Within (d_1)	Between (d_2)	Within (d_1)	Between (d_2)	Within (d_1)	Between (d_2)
d_J	0.2748 ± 0.0693	0.3500 ± 0.0741	0.3291 ± 0.1501	0.4455 ± 0.1352	0.2482 ± 0.0743	0.3428 ± 0.0766
d_H	1.1038 ± 0.5951	1.4910 ± 0.5846	1.5439 ± 1.0098	2.3617 ± 0.8919	0.7881 ± 0.6890	1.2365 ± 0.7095
d_{basin}	0.0582 ± 0.0305	0.0696 ± 0.0272	0.0342 ± 0.0262	0.0436 ± 0.0257	0.0211 ± 0.0160	0.0285 ± 0.0172
d_L	0.3537 ± 0.2076	0.3765 ± 0.2066	0.5056 ± 0.3198	0.5342 ± 0.3120	0.2610 ± 0.2051	0.3036 ± 0.2057

Table 5: Discrepancy between two energy landscapes estimated by the variational Bayes method applied to the MSC data. ‘‘Within’’ and ‘‘Between’’ in the table stand for within-participant and between-participant, respectively. We computed the average and standard deviation of d_1 and d_2 across the participants and across the sessions, respectively.

	Whole-brain network	DMN	CON
d_J	ND = 1.274 $p < 10^{-3}$	ND = 1.354 $p < 10^{-3}$	ND = 1.381 $p < 10^{-3}$
d_H	ND = 1.351 $p < 10^{-3}$	ND = 1.530 $p < 10^{-3}$	ND = 1.569 $p < 10^{-3}$
d_{basin}	ND = 1.196 $p < 10^{-3}$	ND = 1.275 $p < 10^{-3}$	ND = 1.351 $p < 10^{-3}$
d_L	ND = 1.065 $p = 0.0320$	ND = 1.057 $p = 0.0230$	ND = 1.163 $p < 10^{-3}$

Table 6: ND values and the permutation test results for the four discrepancy measures, calculated with the variational Bayes method applied to the MSC data. The p values are the uncorrected values.

those with our original shuffling method schematically shown in Fig. 3.

4. Discussion

We examined test-retest reliability of the energy landscape analysis in terms of four indices. For each index, we calculated a discrepancy in the index value between two estimated energy landscapes. We then constructed and ran a permutation test on the calculated discrepancy value to statistically assess whether within-participant comparison of two energy landscapes yielded a smaller discrepancy value than between-participant comparison of two energy landscapes. For the two data sets, we found significant within-participant test-retest reliability (i.e., within-participant discrepancy being significantly smaller than between-participant discrepancy) in most cases. Furthermore, we found qualitatively the same results for a Bayesian variant of the energy landscape estimation method that enables us to estimate an energy landscape for each scanning session, mitigating the data-hungry nature of the original estimation method.

The accuracy of fit measured by r_D was large for the vari-

	Within (d_1)	Between (d_2)
d_J	0.0784 ± 0.0194	0.1027 ± 0.0232
d_H	0.3145 ± 0.4864	0.3623 ± 0.4967
d_{basin}	0.0309 ± 0.0314	0.0386 ± 0.0325
d_L	0.2535 ± 0.1619	0.2921 ± 0.1783

Table 7: Discrepancy between two energy landscapes estimated by the conventional likelihood maximization method applied to the HCP data. ‘‘Within’’ and ‘‘Between’’ in the table stand for within-participant and between-participant, respectively. We computed the average and standard deviation of d_1 and d_2 across the participants and across the sessions, respectively.

ational Bayes approximation method (i.e., 86.02, 91.50, and 93.51% on average for the whole-brain network, DMN, and CON, respectively) although we did not concatenate the fMRI data across different sessions. These r_D values are close to that with the conventional likelihood maximization method with concatenation of four or five sessions (see Tables 1 and 2). The high accuracy of the variational Bayes method is presumably due to the fact that the target empirical distribution of activity patterns, i.e., $P_N(V_i)$ in Eq. (11), is necessarily different between the two estimation methods. Specifically, $P_N(V_i)$ is the empirical distribution over all sessions for non-Bayesian estimation methods, whereas it is the empirical distribution for one session for Bayesian methods. We do not ascribe the higher accuracy of fit of the variational Bayes method to overfitting. The variational Bayes method yields a Boltzmann distribution for each session. Therefore, it uses $M \times D$ parameters, where we remind that $M = N(N + 1)/2$ is the number of parameters of the Boltzmann distribution and $D = 80$ is the number of sessions. Therefore, it uses D times more parameters than the conventional likelihood maximization method, which uses M parameters to estimate one Boltzmann distribution. However, the variational Bayes method needs to produce an accurate Boltzmann distribution tailored to a single session to attain a high r_D value, which is not the case for the conventional likelihood maximization method. In general, the accuracy of the pairwise MEM simply degrades if the data are shorter (see Tables 1 and 2; also see [38] for a systematic analysis on the effect of the data length on the accuracy). Our results that the variational Bayes

method yields a higher accuracy of fit and higher consistency in the within-participant than between-participant comparison both support that individual-to-individual differences are not negligible when carrying out energy landscape analysis. While such individual differences were a motivation behind the original proposals of the Bayesian methods [40, 70], further comparisons of Bayesian and non-Bayesian estimation methods as well as pursuit of biological and medical relevances of energy landscapes estimated with the Bayesian methods remain future work.

The significance of the test-retest reliability results obtained with the permutation test was similar between the likelihood maximization and variational Bayes methods. However, the ND values were larger for the likelihood maximization than the variational Bayes method. As a separate result, the discrepancy indices were overall smaller for the likelihood maximization than Bayesian method. The latter two results are in favor of the likelihood maximization over Bayesian method for realizing high test-retest reliability. However, we point out that the estimation of an energy landscape for the likelihood maximization requires concatenation of four sessions, whereas the Bayesian method avoids concatenation. Assessment of test-retest reliability for different Bayesian approximation methods [70] and other approximate methods such as the pseudo-likelihood maximization [38, 41], including systematic analysis on the dependence of the results on the data length, is left as future work.

The intraclass correlation coefficient (ICC) has been widely used for investigating test-retest reliability in functional connectivity data [21]. We did not use the ICC because our quantification of the estimated energy landscape was mostly multidimensional and difficult to fit to an ANOVA or similar framework based on which most ICC measures are calculated. Specifically, $\{J_{ij}\}$, based on which we calculated d_J , is a $N(N-1)/2$ -dimensional vector. In addition, we calculated d_H and d_{basin} by examining the activity patterns at local minima and their average over the attractive basin, respectively, in the situation where the number of the local minima varies in one energy landscape from another. Therefore, we decided to calculate a discrepancy measure for each of the four indices between two energy landscapes and constructed a permutation test to examine test-retest reliability. We point out that the average branch length is a scalar characterization of an energy landscape, and therefore it is straightforward to use conventional ICC measures if we discard the normalization factor in Eq. (26). See below for a preliminary analysis of ICCs.

Quantities d_1 and d_2 used for defining ND ($= d_2/d_1$) are averages over 80 and 100 samples, respectively, of a discrepancy measure, such as d_J . For the randomized data produced in the permutation test, averaging over 80 or 100 samples kills fluctuations in individual samples. Therefore, the standard deviations of d_1 and d_2 are small compared to if they were calculated as averages over fewer samples of randomized data. Then, the statistical fluctuation of ND is proportionately small such that ND for the randomized data is centered around 1 with a small standard deviation, which tends to make the ND for the original data significantly different from 1. The number of samples for calculating d_1 or d_2 , such as 80 or 100, is our arbitrary choice,

and the statistical significance of the permutation test depends on the choice of these numbers. This is an important limitation of our permutation test. However, for the present fMRI data, we still obtain qualitatively similar, albeit statistically weaker, results even without carrying out any averaging. We show in Appendix C 11 the ND values for the original data and the p values from the permutation test when d_1 and d_2 are a single sample of a discrepancy measure (e.g., d_J). Tables 11 and 12 indicate that three out of the twelve combinations of the network and the discrepancy measure yield significant p values (i.e., less than $0.05/12 = 0.00417$ uncorrected, considering the Bonferroni correction) for the MSC data when we estimate the energy landscape by the conventional method and the variational Bayes method, respectively. Table 13 also suggests that, out of the four discrepancy measures calculated for the HCP data with the conventional method, one measure yields a significant p value (i.e., less than $0.05/4 = 0.0125$ uncorrected).

As another stress test, we briefly analyzed three measures of ICCs although we have already stated why we did not use them in our main analysis. As mentioned earlier, the average branch length, used for defining d_L , is the only scalar characterization of an energy landscape employed in the present study. Therefore, we computed the average branch length for the whole-brain network obtained from each session of the HCP data and then the first two ICC measures, which are conventional and take a scalar value for each session as input. The third ICC measure assumes vector input for each session, so we use the vectorization of matrix $J = (J_{ij})$. We show the definition of the three ICC measures in Appendix D. The ICC value calculated by a standard method [77] is -0.0115 . In general, negative values of the ICC are interpreted as zero reliability [78, 79]. The ICC value calculated for the average branch length by a second method [80] is 0.4542. This value is reasonably large [80]. We also calculated I_{diff} [23, 25] as an ICC measure. We obtained $I_{\text{diff}} = 10.13\%$ when the data for each participant-session pair is $\{J_{ij}; 1 \leq i < j \leq N\}$. This value is roughly similar to the I_{diff} values for functional networks obtained from the HCP data in a previous study [23]. The results for the last two ICC measures indicate a moderate reliability within a single participant relative to across different participants. In contrast, the first definition of the ICC does not support this result. Although reasons for the discrepancy are unclear, we believe that these preliminary results are a step to in-depth individual-level fingerprinting analyses in the future.

The estimated J matrix can be regarded as a functional connectivity matrix and can be better at estimating the structural connectivity than other conventional definitions of functional connectivity [67]. The estimated h_1, \dots, h_N are close to zero because our standard choice of the threshold (i.e., time average of the signal for each ROI i) makes each σ_i to take -1 and $+1$ approximately with probability $1/2$ each. Then, an energy landscape is almost completely determined by J . In this sense, the reliability of the energy landscapes in terms of the indices we have investigated is caused by the reliability of functional connectivity. However, our results are not direct consequences of known results of high reliability of functional connectivity in fMRI data [18, 20, 25] because they estimated functional con-

nectivity using other conventional methods such as the Pearson correlation coefficient and their variants. Furthermore, which properties of energy landscapes, including J , bear higher reliability is not a trivial question. For example, Table 11 shows that the activity patterns at the local minimum of the energy, measured by d_H , and the activity patterns averaged over the attractive basin, measured by d_{basin} , are more reliable than J for the DMN.

Related to this issue, although we proposed four discrepancy indices for pairs of energy landscapes, they are our arbitrary choices. One can apply the analysis pipeline proposed in the present study to assess test-retest reliability for other discrepancy indices. Other potential discrepancy indices are the frequency of transiting from one particular local minimum to another and features of the transition probability matrix among the activity patterns or among the local minima. Furthermore, our framework of the permutation test on the ND value is not limited to energy landscape analysis (e.g., application to “microstate dynamics” for fMRI data [81]).

Individual variability of fMRI data has most frequently been investigated in terms of functional connectivity [21]. In contrast, we have shown evidence that energy landscape analysis of fMRI data bears session-to-session reproducibility within a participant relative to between different participants. The present results encourage further work toward application of energy landscape analysis to identification of individuals in different cognitive, behavioral, and clinical conditions.

5. Acknowledgements

T.W. acknowledges support from the Japan Society for Promotion of Sciences (TW, 19H03535, 21H05679, 23H04217) N.M. acknowledges support from the Japan Science and Technology Agency (JST) Moonshot R&D (under grant no. JPMJMS2021), the National Science Foundation (under grant no. 2204936), and JSPS KAKENHI (under grant nos. JP 21H04595 and 23H03414).

6. Data availability statement

The two data sets used in this work are publically available. The first data set was provided by the Midnight Scan Club (MSC) project, funded by NIH Grants NS088590, TR000448 (NUFD), MH104592 (DJG), and HD087011 (to the Intellectual and Developmental Disabilities Research Center at Washington University); the Jacobs Foundation (NUFD); the Child Neurology Foundation (NUFD); the McDonnell Center for Systems Neuroscience (NUFD, BLS); the Mallinckrodt Institute of Radiology (NUFD); the Hope Center for Neurological Disorders (NUFD, BLS, SEP); and Dart Neuroscience LLC. This data was obtained from the OpenfMRI database. Its accession number is ds000224. The second data set was provided by the Human Connectome Project, WU-Minn Consortium (Principal Investigators: David Van Essen and Kamil Ugurbil; 1U54MH091657) funded by the 16 NIH Institutes and Centers that support the NIH Blueprint for Neuroscience Research; and

by the McDonnell Center for Systems Neuroscience at Washington University.

7. Ethical approval

All the data were open to the public and collected with the approval of the ethics committees or institutional review board of the recording institutes in the reference [22, 59]. The corresponding author’s institutional review board generally assigns a determination of Not Human Research to such a case.

8. Author’s contribution

TW and NM conceptualized the project. JN, SM, and TW collected the data. PK, JN, SM and TW curated the data. PK, TW, and NM developed the methodology. PK performed formal analysis and investigation. PK and NM validated the results. PK, and NM visualized the results. TW and NM collected the funding. NM administered and supervised the project. PK and NM prepared the first draft of the manuscript and other authors contributed to the manuscript revision. All authors read and approved the final version of the manuscript.

9. Appendix A: Sample disconnectivity graphs

We show a sample disconnectivity graph for the MSC data based on the concatenation of four sessions of a participant the concatenation of four randomized sessions in Fig. 6(a) and (b), respectively.

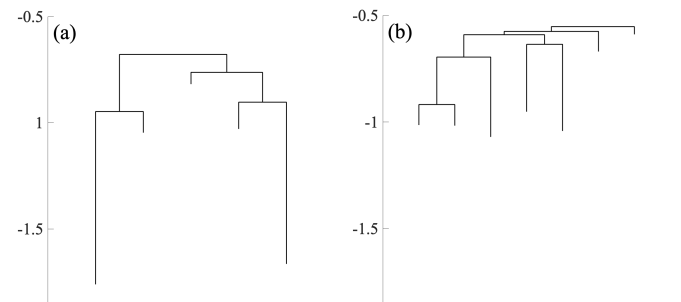


Figure 6: Examples of disconnectivity graphs. (a) Concatenation of the first to the fourth sessions from participant MSC01. (b) Concatenation of the four sessions from the same participant after we randomly shuffle the sessions of the MSC data using the method depicted in Fig. 3. We used the conventional likelihood maximization method.

10. Appendix B: Permutation test by shuffling the participants within each session

In this section, we run the permutation test using a different randomization procedure [75, 76]. We first calculate d_1 and d_2 for the original data in the same way as described in Fig. 3(a) and then the ND value. However, when randomizing the data for the permutation test, we uniformly randomly permute the

fMRI data across participants but within each session. For this randomized data, we calculate d_1 and d_2 , and thus ND. We repeat the randomization followed by the calculation of the ND value $c = 10^3$ times to obtain the p value.

We show the ND values for the original data and the p values from the permutation test for the MSC data combined with the conventional likelihood maximization method, MSC data combined with the variational Bayes method, and HCP data combined with the conventional method in Tables 8, 9, and 10, respectively. We find that the ND values for all the four discrepancy measures and all the three networks are significantly larger than 1 after the Bonferroni correction for the MSC data when combined with the conventional method (i.e., uncorrected $p < 0.05/12 = 0.00417$; see Table 8). When combined with the variational Bayes method, 9 out of the 12 combinations of the discrepancy measure and network yield ND values significantly larger than 1 (see Table 9). The other three combinations still yield $p < 0.05$ before the Bonferroni correction. For the HCP data combined with the conventional method, all the four discrepancy measures are significantly larger than 1 after the Bonferroni correction (i.e., uncorrected $p < 0.05/4 = 0.0125$; Table 10).

	Whole-brain network	DMN	CON
d_J	ND = 1.315 $p < 10^{-3}$	ND = 1.415 $p < 10^{-3}$	ND = 1.580 $p < 10^{-3}$
d_H	ND = 1.934 $p < 10^{-3}$	ND = 3.200 $p < 10^{-3}$	ND = 1.730 $p < 10^{-3}$
d_{basin}	ND = 1.491 $p < 10^{-3}$	ND = 2.359 $p < 10^{-3}$	ND = 1.503 $p < 10^{-3}$
d_L	ND = 1.237 $p = 0.003$	ND = 1.744 $p = 0.001$	ND = 1.609 $p < 10^{-3}$

Table 8: ND values and the permutation test results, calculated with the conventional method applied to the MSC data and the data randomly shuffled across participants but within each session. The p values are the uncorrected values.

	Whole-brain network	DMN	CON
d_J	ND = 1.274 $p < 10^{-3}$	ND = 1.354 $p < 10^{-3}$	ND = 1.381 $p < 10^{-3}$
d_H	ND = 1.351 $p < 10^{-3}$	ND = 1.530 $p < 10^{-3}$	ND = 1.569 $p < 10^{-3}$
d_{basin}	ND = 1.196 $p < 10^{-3}$	ND = 1.275 $p < 10^{-3}$	ND = 1.351 $p = 0.012$
d_L	ND = 1.065 $p = 0.014$	ND = 1.057 $p = 0.034$	ND = 1.163 $p < 10^{-3}$

Table 9: ND values and the permutation test results, calculated with the variational Bayes method applied to the MSC data and the data randomly shuffled across participants but within each session. The p values are the uncorrected values.

d_J	d_H	d_{basin}	d_L
ND = 1.310 $p < 10^{-3}$	ND = 1.152 $p < 10^{-3}$	ND = 1.249 $p < 10^{-3}$	ND = 1.152 $p < 10^{-3}$

Table 10: ND values and the permutation test results, calculated with the conventional method applied to the HCP data and the data randomly shuffled across participants but within each session. The p values are the uncorrected values.

11. Appendix C: Permutation test when d_1 and d_2 are calculated on the basis of one sample

In this section, we run the same permutation test for the MSC and HCP data, but when d_1 and d_2 are just one sample of the discrepancy measure (e.g., d_J). Therefore, for the original data, we only used one participant to calculate d_1 and one session (e.g., the first session from each participant) to calculate d_2 . We show the corresponding ND values for the original data and the p values obtained from the permutation test in Table 11. We applied the conventional likelihood maximization method to the MSC data. We find that the ND value is significantly larger than 1 after the Bonferroni correction (i.e., uncorrected $p < 0.05/12 = 0.00417$) for d_H and d_{basin} in the DMN and d_J in the CON.

	Whole-brain network	DMN	CON
d_J	ND = 1.404 $p = 0.341$	ND = 1.320 $p = 0.386$	ND = 1.288 $p = 0.004$
d_H	ND = 1.518 $p = 0.093$	ND = 2.606 $p < 10^{-3}$	ND = 1.440 $p = 0.167$
d_{basin}	ND = 1.332 $p = 0.210$	ND = 2.5257 $p < 10^{-3}$	ND = 1.259 $p = 0.222$
d_L	ND = 1.015 $p = 0.292$	ND = 1.4165 $p = 0.020$	ND = 1.3769 $p = 0.061$

Table 11: ND values and the permutation test results when we obtain d_1 and d_2 from just one sample of the discrepancy measure value, calculated with the conventional method applied to the MSC data. The p values are the uncorrected values.

We show in Table 12 the corresponding results for the variational Bayes method applied to the MSC data. We find that the ND value is significantly larger than 1 after the Bonferroni correction for d_H in the DMN and CON, and d_L in the CON.

	Whole-brain network	DMN	CON
d_J	ND = 1.067 $p = 0.317$	ND = 1.314 $p = 0.052$	ND = 1.439 $p = 0.005$
d_H	ND = 1.022 $p = 0.438$	ND = 1.641 $p = 0.002$	ND = 2.246 $p = 0.002$
d_{basin}	ND = 1.002 $p = 0.441$	ND = 1.019 $p = 0.091$	ND = 1.001 $p = 0.448$
d_L	ND = 1.1591 $p = 0.305$	ND = 1.2401 $p = 0.1540$	ND = 2.9438 $p = 0.002$

Table 12: ND values and the permutation test results when we obtain d_1 and d_2 from just one sample of the discrepancy measure value, calculated with the variational Bayes method applied to the MSC data. The p values are the uncorrected values.

We show the results for the conventional likelihood maximization method applied to the HCP data in Table 13. We find that ND value is significantly larger than 1 after the Bonferroni correction only for d_J .

d_J	d_H	d_{basin}	d_L
ND = 1.563 $p = 0.002$	ND = 3.382 $p = 0.141$	ND = 1.028 $p = 0.140$	ND = 1.197 $p = 0.321$

Table 13: ND values and the permutation test results when we obtain d_1 and d_2 from just one sample of the discrepancy measure value, calculated with the conventional method applied to the HCP data. The p values are the uncorrected values.

12. Appendix D: ICC measures

We computed the following three ICC measures for the whole-brain network obtained from the HCP data.

We denote by $L_{p,s}$ the average branch length for the s th session of the p th participant, where $p \in \{1, \dots, N_p\}$, $s \in \{1, \dots, N_s\}$, $N_p = 87$ is the number of participants, and $N_s = 4$ is the number of sessions per participant. We calculate the first two ICC measures for the average branch length. We interpret $(L_{p,s})$ as an $N_p \times N_s$ matrix, in which each row represents a participant and each column represents a session. As the first ICC measure, we use [77]

$$\text{ICC} = \frac{\text{MS}_R - \text{MS}_E}{\text{MS}_R + \frac{\text{MS}_C - \text{MS}_E}{N_p}}. \quad (27)$$

In Eq. (27), $\text{MS}_R = \text{SS}_B / (N_p - 1)$ is the mean square for rows, SS_B is the variability between participants (also known as the sum of squares between participants), $\text{MS}_E = \text{SS}_E / (N_p N_s - 1)$ is the mean square for error, SS_E is the residual variability for error (also known as the sum of squares for error), $\text{MS}_C = \text{SS}_C / (N_s - 1)$ is the mean square for columns, and SS_C is the variability between sessions (also known as the sum of squares for columns). We calculate SS_B , SS_E , and SS_C using ExpDes, which is an R package for ANOVA and experimental designs [82].

To calculate the second ICC, we start by calculating the mean of the average branch length over four sessions for each participant p as follows:

$$L(p) = \frac{1}{N_s} \sum_{s=1}^{N_s} L_{p,s}. \quad (28)$$

We also calculate the mean of $L_{p,s}$ over all the $N_p N_s$ participant-session pairs as follows:

$$\langle L_{p,s} \rangle = \frac{1}{N_p N_s} \sum_{p=1}^{N_p} \sum_{s=1}^{N_s} L_{p,s}. \quad (29)$$

The between-participant variability, denoted by $\sigma_{\text{participant}}^2$, is given by

$$\sigma_{\text{participant}}^2 = \frac{1}{N_p} \sum_{p=1}^{N_p} [L(p) - \langle L_{p,s} \rangle]^2. \quad (30)$$

The ICC is given by [80]

$$\text{ICC} = \frac{\sigma_{\text{participant}}^2}{\sigma_{\text{total}}^2}, \quad (31)$$

where σ_{total}^2 is the total variance over all the $N_p N_s$ participant-session pairs and given by

$$\sigma_{\text{total}}^2 = \frac{1}{N_p N_s} \sum_{p=1}^{N_p} \sum_{s=1}^{N_s} (L_{p,s} - \langle L_{p,s} \rangle)^2. \quad (32)$$

The ICC ranges from 0 to 1 and is larger when the different participants are more distinct from each other in terms of $L_{p,s}$.

The third ICC measure that we use is defined in [23, 25] as follows. Let \bar{A} be the so-called identifiability matrix. The (i, j) element of the $N_p \times N_p$ matrix $\bar{A} = (\bar{A}_{ij})$ is the average Pearson correlation coefficient between the i th and j th participant. Specifically, to calculate \bar{A}_{ii} , we first calculate the Pearson correlation coefficient between vector $\{J_{ij}; 1 \leq i < j \leq N\}$ for the s th session of the i th participant and the same vector for the s' th session of the i th participant, where $s, s' \in \{1, \dots, 4\}$ and $s \neq s'$. Then, we average the calculated correlation coefficient over all the $4 \times 3/2 = 6$ session pairs (s, s') , which gives \bar{A}_{ii} . To calculate \bar{A}_{ij} for $i \neq j$, we first calculate the Pearson correlation coefficient between the s th session of the i th participant and the s' th session of the j th participant for each $s, s' \in \{1, \dots, 4\}$. Then, we average the calculated correlation coefficient over all the $4 \times 4 = 16$ session pairs (s, s') , which gives \bar{A}_{ij} . Next, we refer to $I_{\text{self}} \equiv \sum_{i=1}^{N_p} \bar{A}_{ii}/N_p$ as self identifiability. Similarly, $I_{\text{others}} = \sum_{i,j=1}^{N_p} \bar{A}_{ij}/[N_p(N_p - 1)/2]$

represents the average of the off-diagonal elements of the identifiability matrix. We define the differential identifiability by

$$I_{\text{diff}} \equiv (I_{\text{self}} - I_{\text{others}}) \times 100. \quad (33)$$

References

- [1] G. Deco, V. K. Jirsa, P. A. Robinson, M. Breakspear, K. Friston, The dynamic brain: from spiking neurons to neural masses and cortical fields, *PLoS Computational Biology* 4 (2008) e1000092.
- [2] G. Deco, V. K. Jirsa, A. R. McIntosh, Emerging concepts for the dynamical organization of resting-state activity in the brain, *Nature Reviews Neuroscience* 12 (2011) 43–56.
- [3] M. I. Rabinovich, K. J. Friston, P. Varona, *Principles of Brain Dynamics: Global State Interactions*, MIT Press, Cambridge, MA, 2012.
- [4] M. Breakspear, J. A. Roberts, J. R. Terry, S. Rodrigues, N. Mahant, P. A. Robinson, A unifying explanation of primary generalized seizures through nonlinear brain modeling and bifurcation analysis, *Cerebral Cortex* 16 (2006) 1296–1313.
- [5] M. Breakspear, S. Heitmann, A. Daffertshofer, Generative models of cortical oscillations: neurobiological implications of the Kuramoto model, *Frontiers in Human Neuroscience* 4 (2010) 190.
- [6] P. Sanz Leon, S. A. Knock, M. M. Woodman, L. Domide, J. Mersmann, A. R. McIntosh, V. Jirsa, The Virtual Brain: A simulator of primate brain network dynamics, *Frontiers in Neuroinformatics* 7 (2013) 10.
- [7] G. T. Einevoll, C. Kayser, N. K. Logothetis, S. Panzeri, Modelling and analysis of local field potentials for studying the function of cortical circuits, *Nature Reviews Neuroscience* 14 (2013) 770–785.
- [8] K. J. Friston, L. Harrison, W. Penny, Dynamic causal modelling, *NeuroImage* 19 (2003) 1273–1302.
- [9] S. J. Kiebel, M. I. Garrido, R. J. Moran, K. J. Friston, Dynamic causal modelling for EEG and MEG, *Cognitive Neurodynamics* 2 (2008) 121–136.
- [10] O. Sporns, *Networks of the Brain*, MIT press, Cambridge, MA, 2016.
- [11] D. S. Bassett, O. Sporns, Network neuroscience, *Nature Neuroscience* 20 (2017) 353–364.
- [12] R. M. Hutchison, T. Womelsdorf, E. A. Allen, P. A. Bandettini, V. D. Calhoun, M. Corbetta, S. Della Penna, J. H. Duyn, G. H. Glover, J. Gonzalez-Castillo, et al., Dynamic functional connectivity: promise, issues, and interpretations, *NeuroImage* 80 (2013) 360–378.
- [13] V. D. Calhoun, R. Miller, G. Pearson, T. Adalı, The chronnectome: time-varying connectivity networks as the next frontier in fMRI data discovery, *Neuron* 84 (2014) 262–274.
- [14] M. Filippi, E. G. Spinelli, C. Cividini, F. Agosta, Resting state dynamic functional connectivity in neurodegenerative conditions: a review of magnetic resonance imaging findings, *Frontiers in Neuroscience* 13 (2019) 657.
- [15] A. P. Baker, M. J. Brookes, I. A. Rezek, S. M. Smith, T. Behrens, P. J. P. Smith, M. Woolrich, Fast transient networks in spontaneous human brain activity, *eLife* 3 (2014) e01867.
- [16] D. Vidaurre, L. T. Hunt, A. J. Quinn, B. A. Hunt, M. J. Brookes, A. C. Nobre, M. W. Woolrich, Spontaneous cortical activity transiently organises into frequency specific phase-coupling networks, *Nature Communications* 9 (2018) 2987.
- [17] T. Ezaki, Y. Himeno, T. Watanabe, N. Masuda, Modelling state-transition dynamics in resting-state brain signals by the hidden Markov and Gaussian mixture models, *European Journal of Neuroscience* 54 (2021) 5404–5416.
- [18] E. S. Finn, X. Shen, D. Scheinost, M. D. Rosenberg, J. Huang, M. M. Chun, X. Papademetris, R. T. Constable, Functional connectome fingerprinting: identifying individuals using patterns of brain connectivity, *Nature Neuroscience* 18 (2015) 1664–1671.
- [19] J. S. Anderson, M. A. Ferguson, M. Lopez-Larson, D. Yurgelun-Todd, Reproducibility of single-subject functional connectivity measurements, *American Journal of Neuroradiology* 32 (2011) 548–555.
- [20] O. Miranda-Dominguez, B. D. Mills, S. D. Carpenter, K. A. Grant, C. D. Kroenke, J. T. Nigg, D. A. Fair, Connectotyping: model based fingerprinting of the functional connectome, *PLoS ONE* 9 (2014) e111048.
- [21] S. Noble, D. Scheinost, R. T. Constable, A decade of test-retest reliability of functional connectivity: A systematic review and meta-analysis, *NeuroImage* 203 (2019) 116157.
- [22] E. M. Gordon, T. O. Laumann, A. W. Gilmore, D. J. Newbold, D. J. Greene, J. J. Berg, M. Ortega, C. Hoyt-Drazen, C. Gratton, H. Sun, et al., Precision functional mapping of individual human brains, *Neuron* 95 (2017) 791–807.
- [23] E. Amico, J. Goñi, The quest for identifiability in human functional connectomes, *Scientific Reports* 8 (2018) 8254.
- [24] M. Venkatesh, J. Jaja, L. Pessoa, Comparing functional connectivity matrices: A geometry-aware approach applied to participant identification, *NeuroImage* 207 (2020) 116398.
- [25] B. Chiêm, K. Abbas, E. Amico, D. A. Duong-Tran, F. Crevecoeur, J. Goñi, Improving functional connectome fingerprinting with degree-normalization, *Brain Connectivity* 12 (2022) 180–192.
- [26] J. Nakuci, N. Wasylshyn, M. Cieslak, J. C. Elliott, K. Bansal, B. Giesbrecht, S. T. Grafton, J. M. Vettel, J. O. Garcia, S. F. Muldoon, Within-subject reproducibility varies in multi-modal, longitudinal brain networks, *Scientific Reports* 13 (2023) 6699.
- [27] B. van der Velde, R. Haartsen, C. Kemner, Test-retest reliability of EEG network characteristics in infants, *Brain and Behavior* 9 (2019) e01269.
- [28] P. Garcés, M. C. Martín-Buro, F. Maestú, Quantifying the test-retest reliability of magnetoencephalography resting-state functional connectivity, *Brain Connectivity* 6 (2016) 448–460.
- [29] F. T. Candelaria-Cook, M. E. Schendel, C. J. Ojeda, J. R. Bustillo, J. M. Stephen, Reduced parietal alpha power and psychotic symptoms: test-retest reliability of resting-state magnetoencephalography in schizophrenia and healthy controls, *Schizophrenia Research* 215 (2020) 229–240.
- [30] E. A. Allen, E. Damaraju, S. M. Plis, E. B. Erhardt, T. Eichele, V. D. Calhoun, Tracking whole-brain connectivity dynamics in the resting state, *Cerebral Cortex* 24 (2014) 663–676.
- [31] S. Ryali, K. Supekar, T. Chen, J. Kochalka, W. Cai, J. Nicholas, A. Padmanabhan, V. Menon, Temporal dynamics and developmental maturation of salience, default and central-executive network interactions revealed by variational Bayes hidden Markov modeling, *PLoS Computational Biology* 12 (2016) e1005138.
- [32] J. Taghia, S. Ryali, T. Chen, K. Supekar, W. Cai, V. Menon, Bayesian switching factor analysis for estimating time-varying functional connectivity in fMRI, *NeuroImage* 155 (2017) 271–290.

- [33] S. F. Nielsen, M. N. Schmidt, K. H. Madsen, M. Mørup, Predictive assessment of models for dynamic functional connectivity, *NeuroImage* 171 (2018) 116–134.
- [34] C. Yan, D. Liu, Y. He, Q. Zou, C. Zhu, X. Zuo, X. Long, Y. Zang, Spontaneous brain activity in the default mode network is sensitive to different resting-state conditions with limited cognitive load, *PLoS ONE* 4 (2009) e5743.
- [35] B. Rashid, E. Damaraju, G. D. Pearlson, V. D. Calhoun, Dynamic connectivity states estimated from resting fMRI identify differences among schizophrenia, bipolar disorder, and healthy control subjects, *Frontiers in Human Neuroscience* 8 (2014) 897.
- [36] T. Watanabe, S. Hirose, H. Wada, Y. Imai, T. Machida, I. Shirouzu, S. Konishi, Y. Miyashita, N. Masuda, Energy landscapes of resting-state brain networks, *Frontiers in Neuroinformatics* 8 (2014) 12.
- [37] T. Watanabe, N. Masuda, F. Megumi, R. Kanai, G. Rees, Energy landscape and dynamics of brain activity during human bistable perception, *Nature Communications* 5 (2014) 4765.
- [38] T. Ezaki, T. Watanabe, M. Ohzeki, N. Masuda, Energy landscape analysis of neuroimaging data, *Philosophical Transactions of the Royal Society A* 375 (2017) 20160287.
- [39] T. Watanabe, Causal roles of prefrontal cortex during spontaneous perceptual switching are determined by brain state dynamics, *eLife* 10 (2021) e69079.
- [40] J. Kang, S.-O. Jeong, C. Pae, H.-J. Park, Bayesian estimation of maximum entropy model for individualized energy landscape analysis of brain state dynamics, *Human Brain Mapping* 42 (2021) 3411–3428.
- [41] T. Ezaki, E. Fonseca dos Reis, T. Watanabe, M. Sakaki, N. Masuda, Closer to critical resting-state neural dynamics in individuals with higher fluid intelligence, *Communications Biology* 3 (2020) 52.
- [42] T. Ezaki, M. Sakaki, T. Watanabe, N. Masuda, Age-related changes in the ease of dynamical transitions in human brain activity, *Human Brain Mapping* 39 (2018) 2673–2688.
- [43] T. Watanabe, G. Rees, Brain network dynamics in high-functioning individuals with autism, *Nature Communications* 8 (2017) 16048.
- [44] D. Klepl, F. He, M. Wu, M. De Marco, D. J. Blackburn, P. G. Sarriannis, Characterising Alzheimer’s disease with EEG-based energy landscape analysis, *IEEE Journal of Biomedical and Health Informatics* 26 (2021) 992–1000.
- [45] J. D. Allen, S. Varanasi, E. Hong, F.-S. Choa, Energy landscape analysis of fMRI data from Schizophrenic and healthy subjects, in: *Signal Processing, Sensor/Information Fusion, and Target Recognition*, Vol. 11756, SPIE, 2021, pp. 258–266.
- [46] U. Braun, A. Harneit, G. Pergola, T. Menara, A. Schäfer, R. F. Betzel, Z. Zang, J. I. Schweiger, X. Zhang, K. Schwarz, et al., Brain network dynamics during working memory are modulated by dopamine and diminished in schizophrenia, *Nature Communications* 12 (2021) 3478.
- [47] J. Udall, F.-S. Choa, Comparing energy levels in brain regions of interest in ADHD subjects, in: *Smart Biomedical and Physiological Sensor Technology XIV*, Vol. 12123, SPIE, 2022, pp. 47–62.
- [48] D. Krzemiński, N. Masuda, K. Hamandi, K. D. Singh, B. Routley, J. Zhang, Energy landscape of resting magnetoencephalography reveals fronto-parietal network impairments in epilepsy, *Network Neuroscience* 4 (2020) 374–396.
- [49] E. Schneidman, S. Still, M. J. Berry, W. Bialek, Network information and connected correlations, *Physical Review Letters* 91 (2003) 238701.
- [50] E. Schneidman, M. J. Berry, R. Segev, W. Bialek, Weak pairwise correlations imply strongly correlated network states in a neural population, *Nature* 440 (2006) 1007–1012.
- [51] J. Shlens, G. D. Field, J. L. Gauthier, M. I. Grivich, D. Petrusca, A. Sher, A. M. Litke, E. Chichilnisky, The structure of multi-neuron firing patterns in primate retina, *Journal of Neuroscience* 26 (2006) 8254–8266.
- [52] F.-C. Yeh, A. Tang, J. P. Hobbs, P. Hottoway, W. Dabrowski, A. Sher, A. Litke, J. M. Beggs, Maximum entropy approaches to living neural networks, *Entropy* 12 (2010) 89–106.
- [53] P. Khanra, Energy landscape analysis, GitHub repository, Accessed Date: August 18, 2023. URL https://github.com/pitambarkhanra/energy_landscape_analysis.
- [54] J. D. Power, A. L. Cohen, S. M. Nelson, G. S. Wig, K. A. Barnes, J. A. Church, A. C. Vogel, T. O. Laumann, F. M. Miezin, B. L. Schlaggar, et al., Functional network organization of the human brain, *Neuron* 72 (2011) 665–678.
- [55] D. A. Fair, A. L. Cohen, J. D. Power, N. U. Dosenbach, J. A. Church, F. M. Miezin, B. L. Schlaggar, S. E. Petersen, Functional brain networks develop from a “local to distributed” organization, *PLoS Computational Biology* 5 (2009) e1000381.
- [56] K. Murphy, M. D. Fox, Towards a consensus regarding global signal regression for resting state functional connectivity MRI, *NeuroImage* 154 (2017) 169–173.
- [57] K. M. Aquino, B. D. Fulcher, L. Parkes, K. Sabarodin, A. Fornito, Identifying and removing widespread signal deflections from fMRI data: Re-thinking the global signal regression problem, *NeuroImage* 212 (2020) 116614.
- [58] J. Li, T. Bolt, D. Bzdok, J. S. Nomi, B. T. Yeo, R. N. Spreng, L. Q. Uddin, Topography and behavioral relevance of the global signal in the human brain, *Scientific Reports* 9 (2019) 14286.
- [59] D. C. Van Essen, S. M. Smith, D. M. Barch, T. E. Behrens, E. Yacoub, K. Ugurbil, W.-M. H. Consortium, The WU-Minn human connectome project: an overview, *NeuroImage* 80 (2013) 62–79.
- [60] M. F. Glasser, S. N. Sotiropoulos, J. A. Wilson, T. S. Coalson, B. Fischl, J. L. Andersson, J. Xu, S. Jbabdi, M. Webster, J. R. Polimeni, et al., The minimal preprocessing pipelines for the Human Connectome Project, *NeuroImage* 80 (2013) 105–124.
- [61] M. Jenkinson, P. Bannister, M. Brady, S. Smith, Improved optimization for the robust and accurate linear registration and motion correction of brain images, *NeuroImage* 17 (2002) 825–841.
- [62] J. D. Power, K. A. Barnes, A. Z. Snyder, B. L. Schlaggar, S. E. Petersen, Spurious but systematic correlations in functional connectivity MRI networks arise from subject motion, *NeuroImage* 59 (2012) 2142–2154.
- [63] G. C. Burgess, S. Kandala, D. Nolan, T. O. Laumann, J. D. Power, B. Adeyemo, M. P. Harms, S. E. Petersen, D. M. Barch, Evaluation of denoising strategies to address motion-correlated artifacts in resting-state functional magnetic resonance imaging data from the human connectome project, *Brain Connectivity* 6 (2016) 669–680.
- [64] J. S. Siegel, A. Mitra, T. O. Laumann, B. A. Seitzman, M. Raichle, M. Corbetta, A. Z. Snyder, Data quality influences observed links between functional connectivity and behavior, *Cerebral Cortex* 27 (2017) 4492–4502.
- [65] N. Tzourio-Mazoyer, B. Landeau, D. Papathanassiou, F. Crivello, O. Etard, N. Delcroix, B. Mazoyer, M. Joliot, Automated anatomical labeling of activations in SPM using a macroscopic anatomical parcellation of the MNI MRI single-subject brain, *NeuroImage* 15 (2002) 273–289.
- [66] A. Schaefer, R. Kong, E. M. Gordon, T. O. Laumann, X.-N. Zuo, A. J. Holmes, S. B. Eickhoff, B. T. Yeo, Local-global parcellation of the human cerebral cortex from intrinsic functional connectivity MRI, *Cerebral Cortex* 28 (2018) 3095–3114.
- [67] T. Watanabe, S. Hirose, H. Wada, Y. Imai, T. Machida, I. Shirouzu, S. Konishi, Y. Miyashita, N. Masuda, A pairwise maximum entropy model accurately describes resting-state human brain networks, *Nature Communications* 4 (2013) 1370.
- [68] G. Deco, M. Senden, V. Jirsa, How anatomy shapes dynamics: a semi-analytical study of the brain at rest by a simple spin model, *Frontiers in Computational Neuroscience* 6 (2012) 68.
- [69] E. T. Jaynes, Information theory and statistical mechanics, *Physical Review* 106 (1957) 620.
- [70] S.-O. Jeong, J. Kang, C. Pae, J. Eo, S. M. Park, J. Son, H.-J. Park, Empirical Bayes estimation of pairwise maximum entropy model for nonlinear brain state dynamics, *NeuroImage* 244 (2021) 118618.
- [71] C. M. Bishop, N. M. Nasrabadi, *Pattern Recognition and Machine Learning*, Springer, Cambridge, MA, 2006.
- [72] E. Maris, R. Oostenveld, Nonparametric statistical testing of EEG-and MEG-data, *Journal of Neuroscience Methods* 164 (2007) 177–190.
- [73] Y. Liu, S. L. Brincat, E. K. Miller, M. E. Hasselmo, A geometric characterization of population coding in the prefrontal cortex and hippocampus during a paired-associate learning task, *Journal of Cognitive Neuroscience* 32 (2020) 1455–1465.
- [74] J. Kang, C. Pae, H.-J. Park, Energy landscape analysis of the subcortical brain network unravels system properties beneath resting state dynamics, *NeuroImage* 149 (2017) 153–164.
- [75] M. Termenon, A. Jaillard, C. Delon-Martin, S. Achard, Reliability of graph analysis of resting state fMRI using test-retest dataset from the Human Connectome Project, *NeuroImage* 142 (2016) 172–187.
- [76] J. Wang, Y. Ren, X. Hu, V. T. Nguyen, L. Guo, J. Han, C. C. Guo, Test-

Reliability of energy landscape analysis of resting-state functional MRI data

- retest reliability of functional connectivity networks during naturalistic fMRI paradigms, *Human Brain Mapping* 38 (2017) 2226–2241.
- [77] T. K. Koo, M. Y. Li, A guideline of selecting and reporting intraclass correlation coefficients for reliability research, *Journal of Chiropractic Medicine* 15 (2016) 155–163.
- [78] J. J. Bartko, The intraclass correlation coefficient as a measure of reliability, *Psychological Reports* 19 (1966) 3–11.
- [79] S. Yokum, C. Bohon, E. Berkman, E. Stice, Test-retest reliability of functional MRI food receipt, anticipated receipt, and picture tasks, *American Journal of Clinical Nutrition* 114 (2021) 764–779.
- [80] S. Noble, D. Scheinost, R. T. Constable, A guide to the measurement and interpretation of fMRI test-retest reliability, *Current Opinion in Behavioral Sciences* 40 (2021) 27–32.
- [81] S. Islam, P. Khanra, J. Nakuci, S. F. Muldoon, T. Watanabe, N. Masuda, State-transition dynamics of resting-state functional magnetic resonance imaging data: model comparison and test-to-retest analysis, *BMC Neuroscience* 25 (2024) 14.
- [82] E. B. Ferreira, P. P. Cavalcanti, D. A. Nogueira, ExpDes: an R package for ANOVA and experimental designs, *Applied Mathematics* 5 (2014) 2952.